**João Paulo Isidoro Ascenso**

Mestrado Integrado em Engenharia Electrotécnica e de Computadores

# Tool for 3D analysis and segmentation of retinal layers in volumetric SD-OCT images

Dissertação para obtenção do Grau de
Mestre em Engenharia Electrotécnica e de Computadores

Orientador: André Damas Mora, Prof. Auxiliar, FCT-UNL

| | Júri: |
|---|---|
| Presidente: | Prof. Doutor José Manuel Fonseca - FCT/UNL |
| Arguente: | Prof. Doutor Pedro Manuel Vieira - FCT/UNL |
| Vogal: | Prof. Doutor André Damas Mora - FCT/UNL |

FACULDADE DE
CIÊNCIAS E TECNOLOGIA
UNIVERSIDADE NOVA DE LISBOA

**Setembro, 2016**

**Tool for 3D analysis and segmentation of retinal layers in volumetric SD-OCT images**

*To my family*

# Acknowledgements

I will start by thanking my supervisor, Professor Dr. André Mora, for the opportunity to develop this work and all the support given throughout its execution. The MITK and ITK community that keep the project growing and give support to all the problems developers face. To all my friends who supported me during this period and my colleges whom I had the pleasure to share the work space with and my girlfriend for always be there for me.

Lastly my family that worked hard to give me the opportunity to follow my studies.

# ABSTRACT

With the development of optical coherence tomography in the spectral domain (SD-OCT), it is now possible to quickly acquire large volumes of images. Typically analyzed by a specialist, the processing of the images is quite slow, consisting on the manual marking of features of interest in the retina, including the determination of the position and thickness of its different layers. This process is not consistent, the results are dependent on the clinician perception and do not take advantage of the technology, since the volumetric information that it currently provides is ignored.

Therefore is of medical and technological interest to make a three-dimensional and automatic processing of images resulting from OCT technology. Only then we will be able to collect all the information that these images can give us and thus improve the diagnosis and early detection of eye pathologies. In addition to the 3D analysis, it is also important to develop visualization tools for the 3D data.

This thesis proposes to apply 3D graphical processing methods to SD-OCT retinal images, in order to segment retinal layers. Also, to analyze the 3D retinal images and the segmentation results, a visualization interface that allows displaying images in 3D and from different perspectives is proposed. The work was based on the use of the Medical Imaging Interaction Toolkit (MITK), which includes other open-source toolkits.

For this study a public database of SD-OCT retinal images will be used, containing about 360 volumetric images of healthy and pathological subjects.

The software prototype allows the user to interact with the images, apply 3D filters for segmentation and noise reduction and render the volume. The detection of three surfaces of the retina is achieved through intensity-based edge detection methods with a mean error in the overall retina thickness of $3.72 \pm 0.3$ pixels.

**Keywords:** retinal SD-OCT; retinal layers; 3D automatic segmentation; 3D visualization; MITK.

# RESUMO

Com o desenvolvimento da tomografia de coerência ótica no domínio espectral (SD-OCT), é hoje possível a aquisição rápida de grandes volumes de imagens. Tipicamente analisadas por um especialista da área, o processamento das mesmas é bastante lento, sendo marcadas manualmente as características de interesse na retina, nomeadamente a definição da posição e espessura das suas diferentes camadas. É ainda pouco consistente, estando em cada resultado implícita a forma de marcação e perceção dos diferentes especialistas. Além disso não tira proveito da tecnologia utilizada, que apresenta informação volumétrica que é ignorada quando feita uma análise dos cortes seccionais.

É portanto de interesse médico e tecnológico fazer um processamento tridimensional e automático das imagens resultantes da tecnologia OCT. Só assim se conseguirá recolher toda a informação que estas imagens nos podem dar e assim melhorar os diagnósticos e deteção prematura de doenças a nível ocular. Além da análise de características numa perspetiva 3D, é também importante a visualização dessa informação.

Este trabalho propõe aplicar métodos de processamento gráfico tridimensional em imagens da retina recolhidas através da técnica SD-OCT e desenvolver uma interface de visualização que permita apresentar as imagens em 3D e sob diferentes perspetivas. O trabalho foi baseado no uso do *Medical Imaging Interaction Toolkit* (MITK), que engloba vários toolkits *opensource*. Para este estudo será usada uma base de dados pública de imagens SD-OCT contendo cerca de 360 imagens de indivíduos saudáveis e com patologias retinianas.

O *software* desenvolvido permite ao utilizador interagir com as imagens, aplicar filtros 3D para a redução de ruído e segmentação e ainda fazer a renderização do volume. É feita a segmentação de três superfícies da retina através de métodos de deteção de limites, onde se consegue um erro médio na espessura total da retina de $3.72 \pm 0.3$ píxeis.

**Palavras-chave:** segmentação 3D, visualização 3D , SD-OCT, camadas da retina, MITK.

# CONTENTS

# List of Figures

# GLOSSARY

**Anisotropic** An object having a physical property that has a different value when measured in different directions. .

**ARMD** Age-related Macular Degeneration.

**CSV** Comma-Separated Values.

**DICOM** Digital Imaging and Communications in Medicine.

**DOCTRAP** Duke OCT Retinal Analysis Program.

**GCL** Ganglion Cell Layer.

**GPU** Graphics Processing Unit.

**ILM** Inner Limiting Membrane.

**INL** Inner Nuclear Layer.

**IPL** Inner Plexiform Layer.

**IS** Inner Segment.

**ITK** Insight Segmentation and Registration Toolkit.

**MCDE** modified curvature diffusion equation.

**MITK** Medical Image Interaction Toolkit.

**MOC** Meta-Object Compiler.

**NFL** Nerve Fiver Layer.

**NRRD** Nearly Raw Raster Data.

**OCT** Optical Coherence Tomography.

**ONL** Outer Nuclear Layer.

**OPL** Outer Plexiform Layer.

**OS** Outer Segment.

**RMS** root mean square.

**ROI** region of interest.

**RPE** Retinal Pigment Epithelium.

**SD-OCT** Spectral Domain OCT.

**TD-OCT** Time Domain OCT.

**VTK** Visualization Toolkit.

CHAPTER 1

# INTRODUCTION

Image is a valuable tool in medicine providing the means for a noninvasive mapping of a subject's anatomy. Magnetic resonance imaging (MRI), digital mammography and computed tomography (CT), are a few examples of technologies that have improved the knowledge of the anatomy for medical research, diagnosis and treatment planning (Pham et al., 2000)

Being in constant use in modern medicine, the large amount of the generated images brings the need for computers to help with their processing and analysis. The time spent by specialists delineating regions of interest and anatomical structures urges the development of computer algorithms that can perform the same task automatically, with high precision and reproducibility. This is possible with the application of segmentation methods that extract meaningful information from the image and facilitate their display in a clinically relevant way. To better understand this information a visual representation is often needed. The visualization of medical data includes a way to interact, process and represent the data. The visualization process begins by acquiring the data, processing it with the application of noise reduction and feature extraction methods for instance, and lastly the data is rendered or displayed.

In the present study, the medical data was acquired by Optical Coherence Tomography (OCT), which is a non-contact medical imaging technology similar to ultrasound and MRI. OCT uses light reflected on the eye to produce detailed cross-sectional and 3D images (Heidelberg Engineering, 2016). Current research in OCT aims to improve its accuracy and precision, reducing the processing time

and manual intervention as well. With the production of quality 3D information, methods to use it in segmentation and visualization must be developed.

Classically, image segmentation is defined as the partitioning of an image into non-overlapping, constituent regions that are homogeneous with respect to some feature such as intensity or texture (Pal and Pal, 1993). Only recently OCT image segmentation has a more dedicated research and remains one of the most difficult and required step in OCT image analysis, because there is no universal segmentation method that will deliver good results in different situations.

Having 3D information available, it is important to make the best use of it to follow the evolution of the acquisition systems. Three-dimensional medical images were usually analyzed as sequences of 2D slices, which lacks contextual information between slices. Performing segmentation in 3D space will give more consistent results, defining object surfaces rather than sets of individual contours.

A correct intraretinal segmentation is an important tool for ophthalmologist to better understand and study pathologies. Several applications of the segmentation can be defined, like volumetric measurements of the scan in defined regions, comparison of retinal thickness during treatment and detection of pathologies that affect the thickness of retinal layers, among others.

The objective of this work is to explore methods of volumetric processing of OCT images in order to identify retinal layers, as well as to develop an interface that enables viewing and interaction with such data. The 3D image can be sliced in any direction but is typically viewed along the anatomical planes. This planes are named axial, sagittal and coronal, being the $(x, y)$, $(y, z)$ and $(x, z)$ Cartesian planes, respectively. Figure 1.1 shows the position of each plane relative to the human skull.

This nomenclature is used along the present work and the images shown in this document relate to this planes. Note that they are a slice of the volume and not an isolated 2D image, so they are representative of the 3D processing results.

The retinal anatomy is presented in the next section, followed by a more in-depth look at OCT technology. Also a presentation of the tools used during development, as well as the image formats in use will be given in the following sub-chapters.

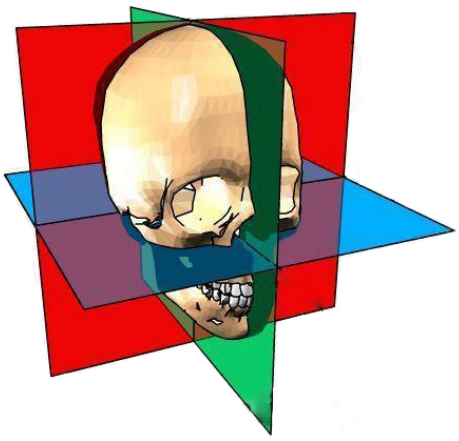

Figure 1.1: Anatomical planes. Axial plane in blue, sagittal in green and coronal in red. Adapted from Anatomia Online (2014)

## 1.1 The retina

Is important to start by introducing the retinal structure to better understand what is seen in the OCT scans.

The retina covers the back of the eye in about 65% of its interior surface. It is responsible to convert the light into signals that are sent to the brain, through the optic nerve. In the middle of the retina a small dimple is found named as fovea. This spot is where the eye has the most color perception and where vision is sharpest. The fovea is the central point in a depression that goes from 2.5 to 3$mm$ in diameter known as macula. All the studied OCT scans are from this region of the retina, identified in figure 1.4.

As represented in the figure 1.2 its structure shows different layers. From the inside to the outside of the eye, the first surface detectable is the limit between the vitreous and the retina. The choroid is the vascular layer of the eye and lies behind the retina. The nomenclature used throughout the document and shown in the figure are as follow:

- Inner Limiting Membrane (ILM)
- Nerve Fiver Layer (NFL)
- Ganglion Cell Layer (GCL)
- Inner Plexiform Layer (IPL)
- Inner Nuclear Layer (INL)
- Outer Plexiform Layer (OPL)
- Outer Nuclear Layer (ONL)
- Inner Segment (IS)
- Outer Segment (OS)
- Retinal Pigment Epithelium (RPE)

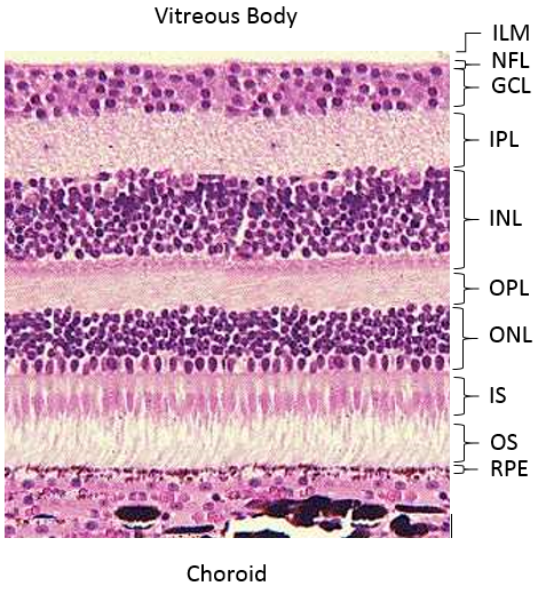


Figure 1.2: Retinal layers observed in a microscope. Adapted from Bristol University (2000).

## 1.2 Age-related Macular Degeneration

According to the World Health Organization (2007), Age-related Macular Degeneration (ARMD) is the leading cause of blindness in the developed world. Usually it produces a slow, painless loss of vision. Ophthalmologists often detect early signs of macular degeneration, before anomalies are detected in a retinal exam.

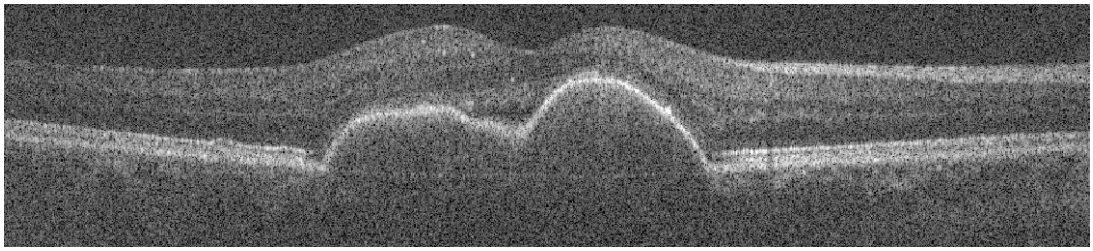

Figure 1.3: SD-OCT scan of a retina with drusen.

ARMD may be divided in two types, wet (exudative) and dry (non-exudative), being the later the most common and characterized as drusen formation and geographic atrophy of the RPE (figure 1.3). Wet AMD presents retinal edema, sub-retinal serous exudation, and eventual scarring of the overlying retina. Drusen are extra-cellular deposits that form between the RPE and innermost layer of the choroid, known as Bruch's membrane, seen on detail in figure 1.4.

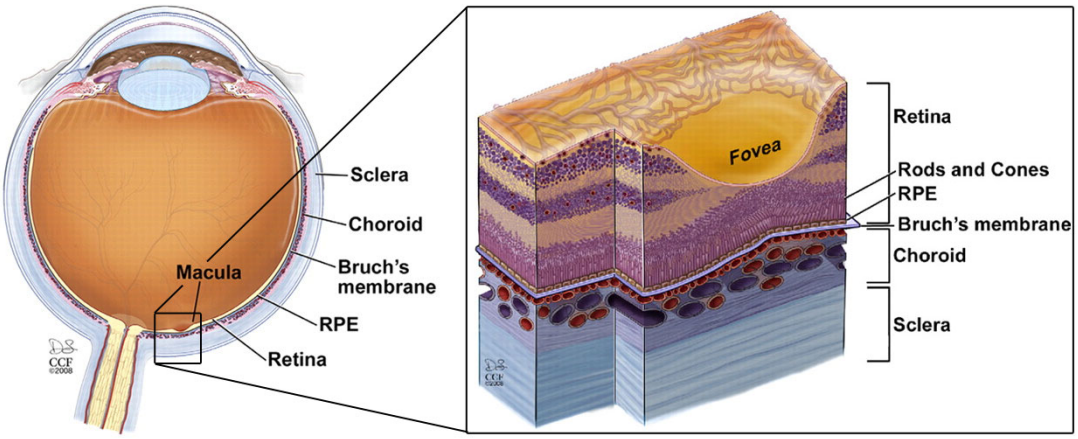


Figure 1.4: Macula position on the eye and detail section of retina (Yuan et al., 2010).

It is possible to observe the retina by photographing it directly through the pupil. This method is called fundus photography (figure 1.5) and is used to diagnose and treat eye diseases. These images are commonly used to follow the development of drusen. Similar to OCT images, the evaluation of this images can be fastidious when done manually, not ensuring coherent results. To solve such problems some automatic classification techniques have also been developed in these type of images. Smith et al. (2005) used the Otsu method to identify drusen after some pre-processing of the image. Mora et al. (2011) presented an automatic drusen detection that achieves similar results to the experts and with a higher reproducibility, using a gradient based segmentation algorithm.

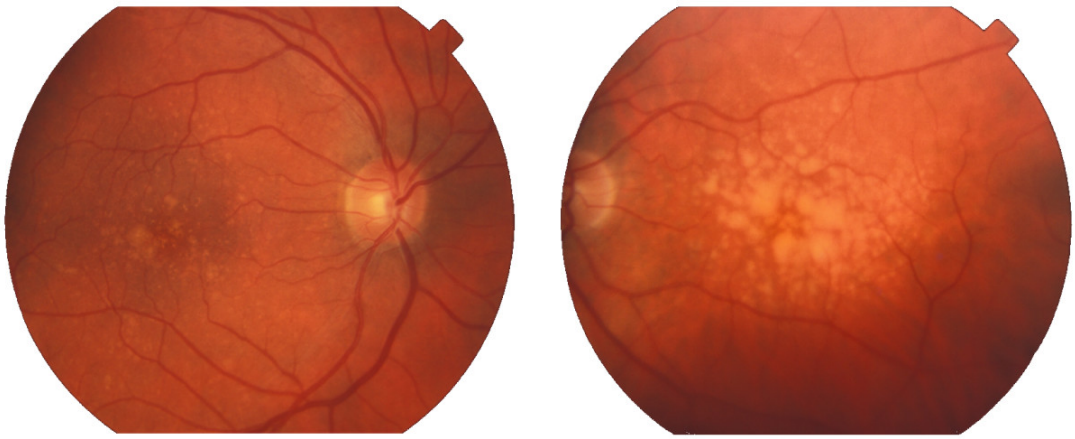

Figure 1.5: Retinal fundus photography showing drusen.

## 1.3 Optical Coherence Tomography - OCT

OCT is a powerful imaging system that produces images based on interference patterns. The development in OCT technology has enable to acquire more data and faster, reaching resolutions in the $\mu$m level and penetration of a few millimeters in scattering media. It has been widely used from material inspection to medical imaging and is very common in the ophthalmology field.

An early version of this technology, Time Domain OCT (TD-OCT), has a moving reference mirror and uses low-coherence interferometry as an indirect measure of the time of travel of the light reflected in the sample. In low-coherence interferometers a light beam is emitted by a source with a broad optical bandwidth and split into two different paths, known as reference and sample arms of the interferometer, reaching then a mirror and the subject to be imaged respectively (figure 1.7(a)). As the mirror moves, the reflected light from each path is guided into a photo-detector, that records the light intensity and analyses the interference effect, used as a relative measure of distance traveled by the light beam. This interference pattern appears when the mirror is nearly at the same distance as the reflecting structure in the sample. The displacement distance of the mirror between the occurrence of interference is the optical distance between two reflecting structures. In case of the retina, it contains layers with different reflection indexes, and the transition between layers causes intensity peaks in the interference pattern. Being a mechanical process, it is relatively slow and limits both the amount of data that can be captured and the image quality.

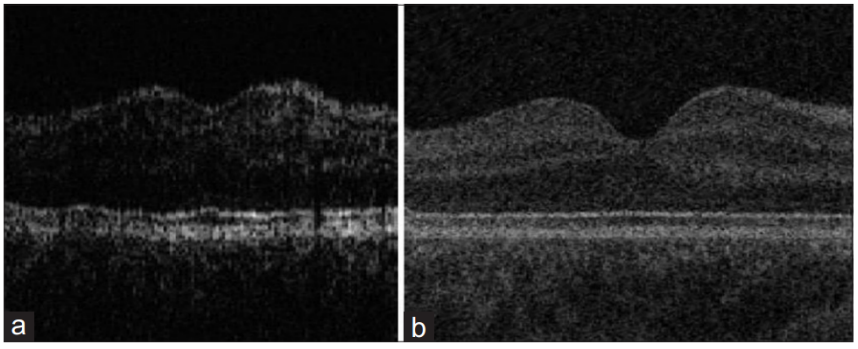


Figure 1.6: Image quality of time domain (a) and spectral domain (b) OCT (Kafieh et al., 2013a)

More recently the Spectral Domain OCT (SD-OCT) was introduced, referenced also as Fourier domain OCT (FD-OCT). This technology solved many of the

problems and limitations of the TD-OCT system. A comparison between the outputs of the two modalities can be seen in figure 1.6. It does not have any moving parts (the reference mirror is fixed), which enables faster acquisition times and higher density. The detection system is now a spectrometer, where intensity is recorded as a function of the light frequency. The resulting intensity modulations are named spectral interference. Each reflecting layer has a different location in the sample, represented by the rate of intensity variation over different frequencies (Wasatch Photonics, 2015).

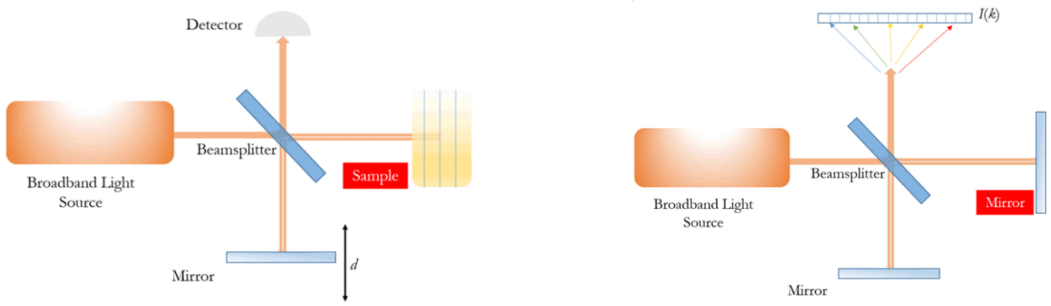


(a) TD-OCT (b) SD-OCT

Figure 1.7: Comparison between the two acquisition techniques (Wasatch Photonics, 2015)

As the light beam hits the sample, its reflection gives information on that particular position, producing an A-scan.

As presented in 1.8, the A-scan is a one dimensional acquisition, that measures the intensity of light back-scattered for different depths in the axial direction. A B-scan is a 2D image obtained by translating acquisition of A-scans in a transverse direction. For last the volumetric scan is a sequence of B-scans, where each one is a slice of the volume in a given position.

In some scans the presence of motion artifacts can be observed, mainly manifested in the axial direction. The improvement of the technology as resulted in faster acquisition times, but that has not been enough to overcome movements of the subject during scans because these higher speeds are used to gather more data and not to reduce the total acquisition time. Newer systems are applying eye tracking methods at acquisition time to avoid these artifacts.

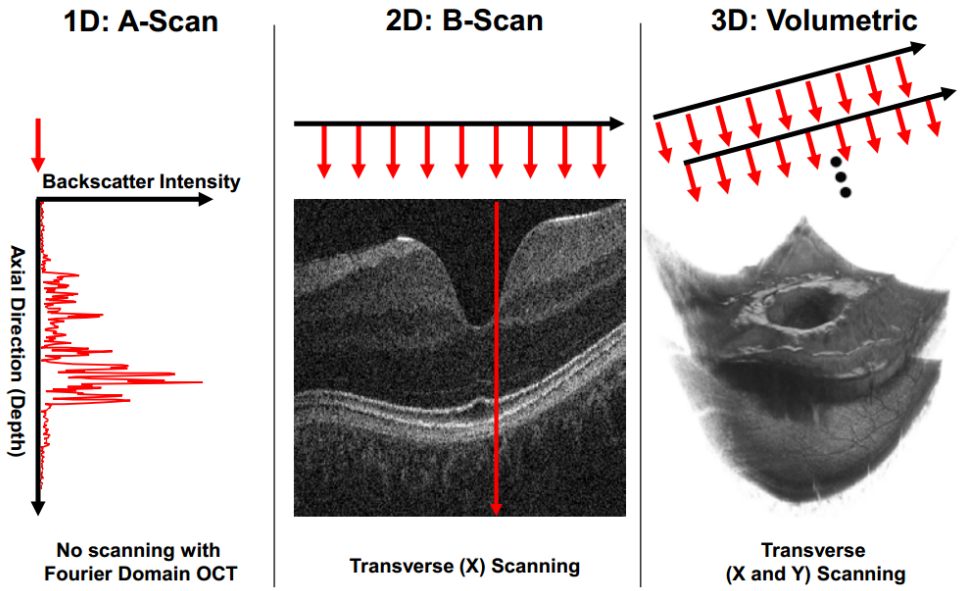


Figure 1.8: OCT scanning schematic (Kraus et al., 1991).

## 1.4 Toolkits

The development of the proposed application relies on the usage of volumetric visualization and processing toolkits, the Visualization Toolkit (VTK) and the Insight Segmentation and Registration Toolkit (ITK) respectively, which are frequently used in 3D medical image visualization. These are currently maintained by Kitware, Inc., a company dedicated to the development and support of open-source software. To integrate both toolkits the Medical Image Interaction Toolkit (MITK) was used, a framework maintained by the German Cancer Research Center, presented below. MITK relies on Qt to provide a dynamic interface. How these toolkits are related can be better understood with the class diagram in figure 1.9. Qmitk is a helper class that merges the high interactivity of MITK with the graphic interface possibilities provided by Qt.

### 1.4.1 The Medical Image Interaction Toolkit - MITK

The Medical Image Interaction Toolkit (MITK) is a free open-source software that facilitates the creation of interactive medical image processing software, allowing the development of applications specifically tailored for a medical task (MITK, 2016). MITK is an object-oriented, cross-platform library implemented in C++. Currently under active development, it aims at supporting the development

of medical imaging software with a high degree of interaction, making it a consistent framework to combine image segmentation, registration and visualization. It combines VTK and ITK and adds important features for developing interactive medical imaging software and that are not covered by any of the others.

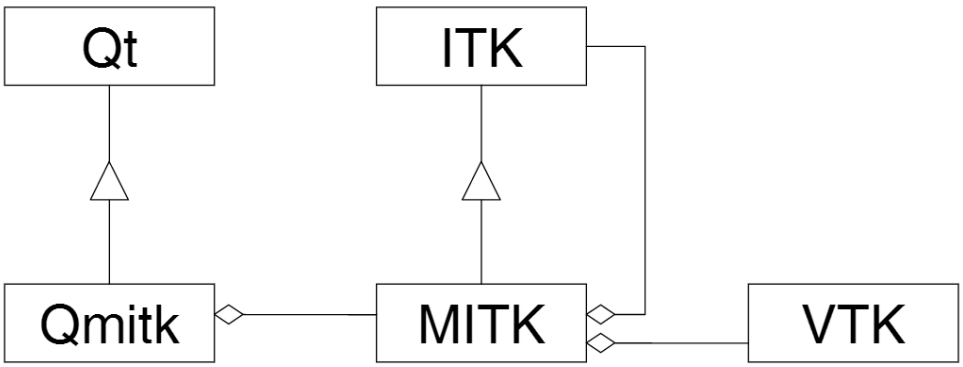


Figure 1.9: Relation of MITK to the toolkits ITK, VTK and Qt

### 1.4.2 Insight Segmentation and Registration Toolkit - ITK

The ITK is a large and complex open-source software toolkit for performance of image registration and segmentation. Its implementation in C++ employs generic programming, using templates, allowing that many of the algorithms can be applied to arbitrary spatial dimensions and pixel types (Johnson and Mccormick, 2014).

### 1.4.3 Visualization Toolkit - VTK

The Visualization Toolkit is an open-source software system for 3D computer graphics, image processing, and visualization. It is a C++ class library that supports a wide variety of visualization algorithms, as well as advanced modeling techniques and offers some 3D interaction widgets. The toolkit supports parallel processing and integrates with various databases on GUI toolkits such as Qt. VTK is used in commercial applications, as well as in research and development (Kitware, 2016).

### 1.4.4 Qt

Qt is a framework for development of applications and graphic user interfaces. Based on intuitive and modularized C++ library classes it is also available in a

open-source. It uses a preprocessor, the Meta-Object Compiler (MOC), to extend the C++ language, including features like signals and slots that connect elements of the interface. The graphic user interface in MITK is based in by this framework (Qt, 2015).

## 1.5 Image Formats

When working with large set of images, some standards are more helpful in managing the files. In the medical field, information about the patient and acquisition conditions are important to keep along with the data that is transferred between medical staff and hospitals.

Below are the two standards used in this project, both allow easy storage and management of the 3D data sets.

### 1.5.1 DICOM

Digital Imaging and Communications in Medicine (DICOM) is the international standard that defines a set of norms for processing, storage, transmission and displaying of medical images as well as derived structured documents (ISO 12052). Created to ensure the interoperability between systems, it allows products to work with present and future imaging modalities, regardless of the vendor.

Used in hospitals worldwide, it is implemented in many imaging devices in fields like radiology, cardiology imaging, radiotherapy, dentistry, ophthalmology and more (NEMA, 2016).

### 1.5.2 NRRD

Nearly Raw Raster Data (NRRD) it is a library and file format intended to support scientific visualization and image processing applications. It works with N-dimensional raster data and is flexible with the type, encoding and endianness. The library also supports PNG, PPM, PGM and some VTK datasets (NRRD, 2016).

## 1.6 Objectives

The objective of this thesis is to make the automatic segmentation of retinal layers in SD-OCT images using 3D processing methods. To present the results it will be

developed a visualization interface, with views from different perspectives and 3D models.

## 1.7 Thesis Structure

This thesis is divided into five chapters organized using the following structure.

On Chapter 2 is presented the state of the art, focusing on previous solutions for the segmentation of OCT images. One of the main problems when dealing with this images is their significant noise, therefore most commonly used methods for noise reduction are presented. On the segmentation techniques, the newest methods and a reference to the older one are presented. Then a brief explanation on surface and volume rendering is given.

Chapter 3 presents all the developed work and methods applied. Going through all the process of segmentation from noise reduction to presentation of the results. In the end of this chapter the developed prototype is presented with an explanation of its basic functionalities.

On Chapter 4 a comparison and validation of the proposed segmentation is made. Using the manual segmentation available it is possible to compare the algorithm to it and evaluate the segmentation error. The results obtained are then compared to the ones presented in previous publications.

Finally in Chapter 5, conclusions are draw and main aspects for future developments are presented.

CHAPTER 2

# STATE OF THE ART

In this chapter the methods that achieve the best results in the processing of retinal OCT images and the most advanced image processing techniques in 3D will be presented. The main challenges are related to noise reduction and efficient and robust segmentation. A recent overview of the techniques that face these problems was made by Baghaie et al. (2014), and also includes a chapter on image registration. Besides the image processing, is essential to display the data and results graphically to better understand them. An overview of visualization of 3D data is made in the last sub-chapter.

## 2.1 Noise Reduction

One of the characteristics of images acquired by narrow band systems like OCT is the presence of speckle noise that reduces contrast and degrades the image in a way that makes detecting the retinal layers a difficult task. This type of granular noise is influenced by backscattering of the beam inside and outside of the sample volume and random propagation delays caused forward scattering. These scattered signals add coherently, creating regions of constructive and destructive interference, that appear as speckle noise in the image (Schmitt et al., 1999).

To face this problem, noise reduction techniques must be applied before any further analysis. However, new acquisition systems with high speed imaging can produce multiple images in the same instant and by averaging them it is possible to reduce the speckle noise.

Noise reduction techniques can be applied during data acquisition, being the compounding techniques one effective way to reduce the speckle noise. These techniques are divided into four main categories: spatial-compounding (Avanaki et al., 2013), angular-compounding (Schmitt, 1997), frequency-compounding (Pircher et al., 2003) and strain-compounding (Kennedy et al., 2010). These compounding methods are usually not preferred since they require multiple scans of the same data. They rely on changing the OCT system with the drawback of increasing the system complexity. Therefore, the use of post-processing techniques is more popular.

The well-known anisotropic diffusion method proposed by Perona and Malik (1990) is used for speckle reduction. The ability in preserving edge information is what makes this filter so popular.

Different variations of it have been made, one of them is the Modified Curvature Anisotropic Diffusion. This method, proposed by Whitaker and Xue (2001) has shown to be more effective than the classic anisotropic diffusion at removing noise, being more aggressive at enhancing edges and less sensitive to contrast. It is based on a level-set equivalent of the equation proposed by Perona and Malik (1990) named modified curvature diffusion equation (MCDE).

The figure 2.1 shows the root mean square (RMS) error as function of the number of iterations of the filter, and confirms the better performance of the MCDE filter.

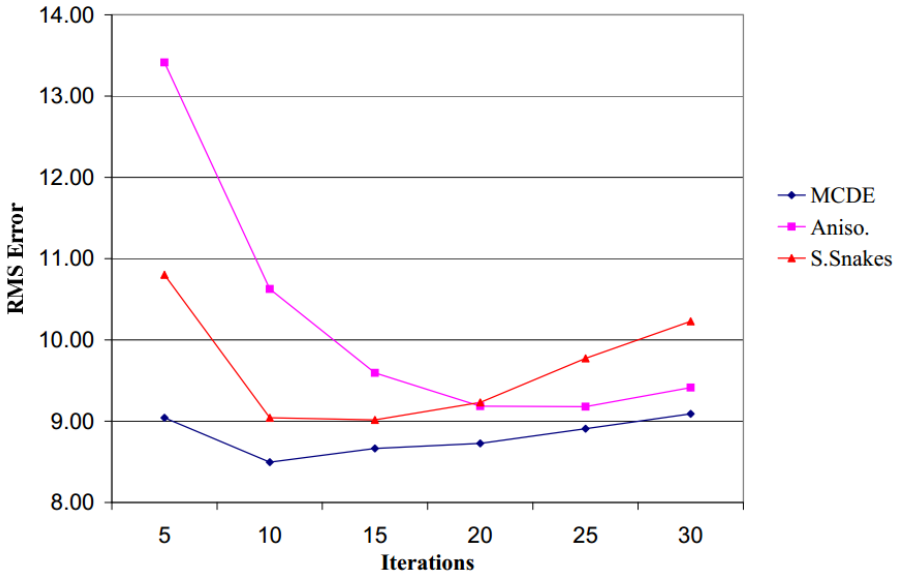


Figure 2.1: RMS error for recovering a noisy image (Whitaker and Xue, 2001)

Salinas and Fernández (2007) compare the one other variation, the complex diffusion filter proposed by Gilboa et al. (2004) with the traditional Perona-Malik filter, which resulted in better speckle noise removal.

Wavelet transform has also been used and showed promising results, but its lack of directionality imposes a limitation on proper denoising images. Other methods using median filters, mean filters, directional filtering, low-pass filtering or 2D smoothing, among others, can be found in literature.

## 2.2 Segmentation

Being one of the most difficult steps in OCT image analysis, segmentation is also the most required. During the last two decades several of methods were proposed. Besides the presence of noise covered in the previous section, other problems are encountered in the segmentation of OCT images (Baghaie et al., 2014) like the variation of intensity within the same layers. Also the shadows caused by blood vessels create holes in the segmented surfaces what affects the performance of the segmentation methods. Finally, the relative motion of the subject, even from breathing or the heart beat, causes motion artifacts that degrade the image.

A typical approach for segmenting retinal layers consist on preprocess the image (with median filter or anisotropic diffusion per example), find features of interest on each A-scan and in some cases correct their discontinuities.

The retinal segmentation methods can be categorized into five classes:

- methods applicable to A-scans;
- intensity-based B-scans analysis;
- active contour approaches;
- analysis methods using artificial intelligence and pattern recognition techniques;
- segmentation methods using 2D/3D graphs constructed from the 2D/3D OCT images.

The method proposed in this work can be classified as a 3D intensity-based solution. Kafieh et al. (2013a) presented a in depth study of segmentation algorithms used in segmentation of the retina. For the purpose of this study more focus will be given to 3D approaches.

There are 3D methods using level-sets and active-shape models that involve converging to a local minimum, not guaranteeing an optimal solution though all image.

Sun and Zhang (2012) proposed a 3D method based on pixel intensity, boundary information and intensity changes on both sides of the layer simultaneously, which can segment the RPE, IS/OS and ILM layer boundaries.

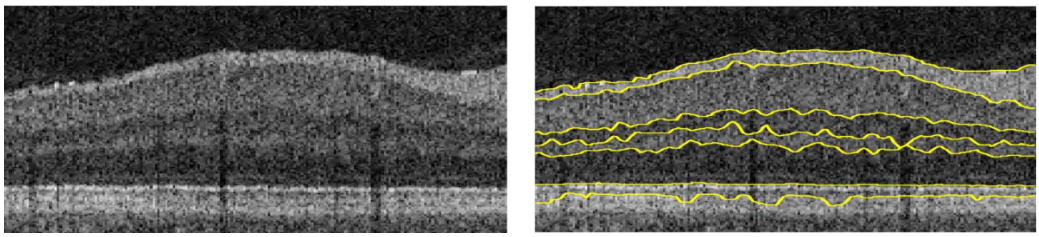

Figure 2.2: Example of the resulting segmentation from Garvin et al. (2009).

One of the most promising techniques in image segmentation uses the theory of graphs (Li et al., 2006). An algorithm proposed by Garvin et al. (2008) transforms a 3D segmentation problem into finding a minimum cost closed set in a vertex-weighted geometric graph. This graph is created from edge and regional image information as well as a definition of surface interaction and smoothness constraints that evaluate the feasibility of a surface. This method guarantees to find the optimal solution with respect to the cost function defined. A similar method as been applied by Chiu et al. (2010), with results seen in figure 2.3, but in a 2D approach and combining dynamic programming what reduced the processing time. Here each B-scan is represented as a graph of nodes and each node corresponds to a pixel that connects to others by links referred as edges. To precisely cut the graph is essential to assign the appropriate edge weights, using metrics as distance between pixels or intensity differences. Finally, the Dijkstra's algorithm is used as an efficient way to find the lowest weighted path on the graph.

Using support vector machines, graph theory, and dynamic programming, Srinivasan et al. (2014) also achieves an accurate segmentation of seven to ten layers.

Niemeijer et al. (2008) developed a method to segment blood vessels in 3D SD-OCT images of the retina, processing the volume slice-by-slice.

Another recent approach was the use of diffusion maps by Kafieh et al. (2013b) what instead of using edge-based information, relies on regional image texture, improving the robustness of the segmentation of low contrast or poor inter-layer gradients cases (figure 2.4). This method can be applied in both 2D and 3D data, presenting better results when detecting the layers position in 3D.

Segmentation has become more integrated with the volume rendering pipeline.

These two processes can't be completely separated (Zhou and Tönnies, 2003). Without visualization, the segmentation results can't be presented.

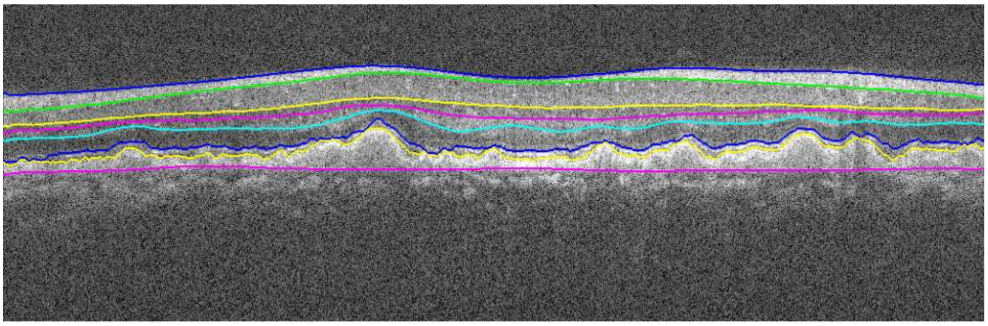

Figure 2.3: Example of the resulting segmentation of 7 layers from a pathological eye by Chiu et al. (2010).

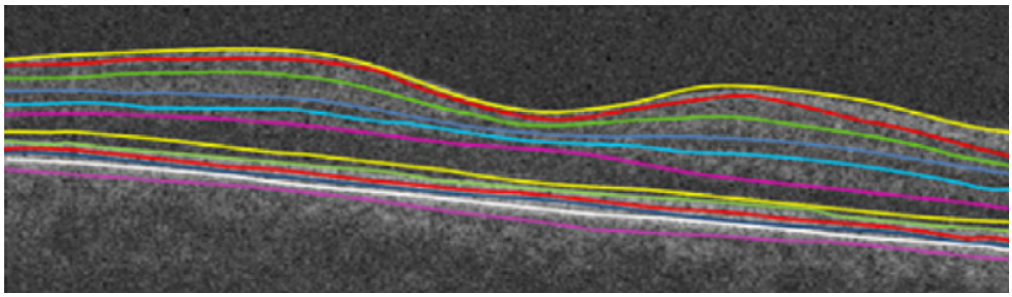

Figure 2.4: Resulting segmentation of 11 layers by Kafieh et al. (2013b)

## 2.3 Volume Rendering

Medical images are often acquired in a set of 2D images, equally spaced between them, which allows their rendering as a volume. Volume rendering, also referred as direct volume rendering or composite rendering, is based on the simulation of light passing through matter with the objective of displaying a 3D image in its entirely (Papademetris and Joshi, 2009). Volume rendering gives better image quality and doesn't define surfaces when generating images. On the down side, since it uses all the voxels of the image, the execution time is proportional to the size of the dataset.

### 2.3.1 Ray Casting

This simulation of light is made by a ray that goes across each pixel, starting from the user's viewpoint and sampling the dataset along its path. The color and opacity

values are defined by transfer functions that adjust the rendering output in order to get desired results. The classic technique known as ray casting, was introduced by Levoy (1988). He defined the following equations which are executed at every point along the ray:

$$C_{i+1} = A_i * C_i + (1 - A_i) * a_i * c_i \tag{2.1}$$

$$A_{i+1} = A_i + (1 - A_i) * a_i \tag{2.2}$$

where $C_i$ stands for the accumulated color along the ray and $A_i$ represents the accumulated opacity along the ray. The current voxel's color and opacity, which is obtained from the transfer function, is respectively $c_i$ and $a_i$. Every time the ray hits a non-zero voxel, the color and opacity are looked up in the transfer function.

There are different ray traversal methods. In the most basic, known as first-hit, the first non-zero voxel found is used to map the volume. The average method computes the average of the voxels's intensity. The Maximum Intensity Projection (MIP), uses the maximum intensity found across the ray. The most common method is called Accumulate. Here the color and opacity are accumulated along the ray path allowing to display multiple surfaces, like skin and bone on the same volume. An example of the resulting volume from each method can be seen in figure 2.5.

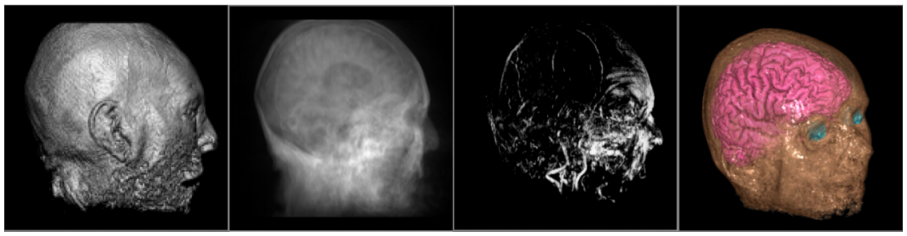

Figure 2.5: Example of the four ray traversal methods. Fist-hit, Average, MIP and Accumulate (Papademetris and Joshi, 2009)

### 2.3.2 Texture Mapping

This technique uses the graphics hardware to render the volume. In 2D texture mapping are used slices parallel to the coordinate planes. Polygons are textured with different slices and blended together, simulating a bi-linear interpolation, to achieve the visual representation of the dataset. It uses a lot of memory since it has 3 stacks of 2D textures, one for each axis.

Three-dimensional texture mapping however allows the data to be loaded into a single 3D texture. Slices are then made parallel to the viewing direction, simulating trilinear interpolation, and since a single data structure is used there is no need to have 3 copies of the same data, saving memory.

### 2.3.3 Other Rendering Techniques

Other techniques like Shear Warp proposed by Lacroute and Levoy (1994) and Splatting proposed by Westover (1990) are also important. Shear warp is recognized as one of the fastest rendering methods, but sacrifices the image quality. Based on three steps, the algorithm starts by shearing and resampling the volume slices, then projects an intermediate image that is finally warped into the final image.

In Splatting techniques the volume is represented by a field of 3D kernels with amplitudes related to the voxel's intensity. The name comes from the similarity to throwing a snowball against a wall. Each kernel leaves a weighted footprint that will accumulate into a image.

A deeper explanation and comparison between the most used volume rendering algorithms is made by Zhou and Tönnies (2003).

## 2.4 Surface Rendering

Unlike volume rendering, surface rendering aims to represent only some features from the total volume, representing boundaries of a structure. The resulting surface is called an isosurface and each surface has a unique value known as iso-value.

One of the most popular surface rendering method is the Marching Cubes, developed by Lorensen and Cline (1987). This method, after having found the surface correspondent to a user defined threshold verifies each voxel in the volume for intersection with the isosurface. To do this it uses a logical cube created from eight pixels from adjacent slices, and analyzes how the surface intersects with it. Fourteen possible patterns of intersections of the surface with the cube were defined, as seen in figure 2.6. Using diverse symmetries of the cubes the 256 possible cases of intersection can be produced. An index is created for each case that allows to identify the intersected edge and to interpolate the surface intersection, producing from 1 to 4 triangles per cube. Finally a unit normal is calculated for each triangle vertex, needed to produce shading on the image.

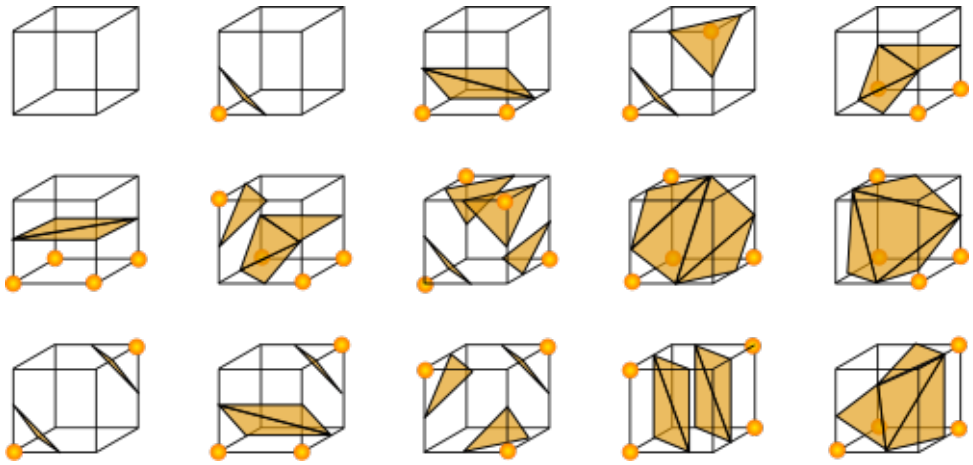

Figure 2.6: Triangulated Cubes (Wikipedia, 2010)

CHAPTER 3

# DEVELOPED WORK

This chapter presents the overall pipeline for the image processing and the methods applied. To implement image processing and visualization tools, the search for the best platform lead to VTK as a popular toolkit for medical image visualization with strong support for 3D data. The following sub chapter presents the challenges faced on using this platform. Then will be presented the steps towards noise reduction, layer segmentation and the graphical user interface prototype.

All 2D images presented throughout the document show slices of the volume in the axial plane, $(x, y)$, unless referenced otherwise. Similar images are used for easy comparability of results from the various filters applied. In binary images the color was inverted to get a clearer visualization when printed. Often the term pixel is used when presenting a slice of the volume, but since all the processing is done with the volume, pixel often refers to voxel.

## 3.1 Software Development Platform

Initially the software was intended to be developed in C# language. The search for the best toolkit for image processing and 3D visualization lead to ITK and VTK, respectively. Even though these are implemented in C++, a few wrappers are available including for C#, named ActiViz.NET and SimpleITK, for VTK and ITK respectively.

A basic interface similar with the presented in section 3.7 was fully implemented in C#. After having an interface, the problem was faced using SimpleITK

since VTK by itself has limited image filtering capabilities. This brought a problem in interconnecting this two wrappers. Even though the basic data being analyzed is the same, each one was its own image type definitions and are not directly interchangeable. A solution was found but incompatibilities kept emerging with further developments what lead to the decision of changing the programming language and start using the toolkits' native one.

This initial effort was helpful by the knowledge gathered about the toolkits, but ended up not having any usage on the final solution. The time spent on this issues delayed the development of the solution.

The work was then developed in C++ using the MITK toolkit, which integrates ITK (v4.7) with VTK (v6.2) and uses the Qt framework for the GUI. It is important to note the size of these toolkits, that can take several hours to build, and their configuration might bring some problems besides the documentation available. The setup of the toolkits was difficult and took some time to make them work without problems.

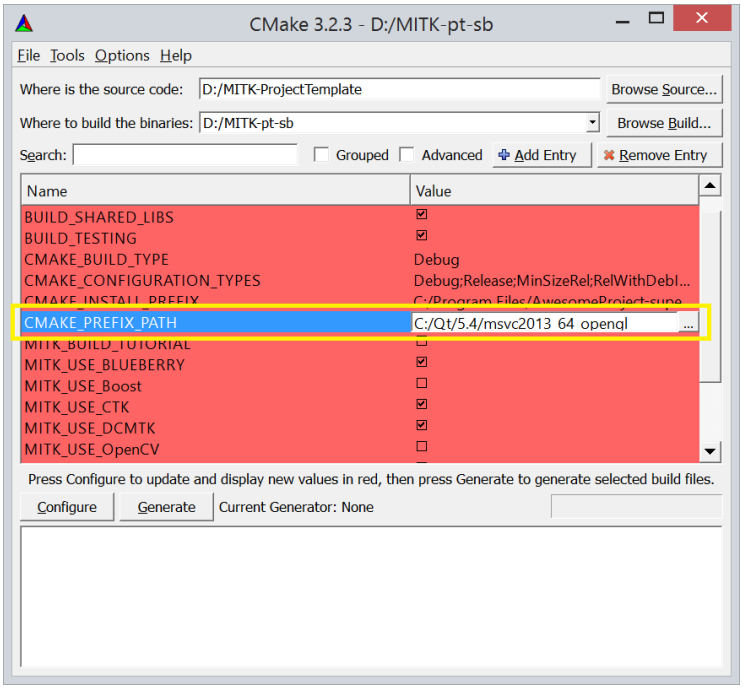


Figure 3.1: CMake configuration window.

The configuration is made through CMake (figure 3.1), a tool designed to build software created by Kitware, Inc. A configuration file must be defined with a set of rules and the interface of the program allows to easily select what to include in the build of the software. MITK has a project template that facilitates the build

of all the toolkit at once, but to build some features that are not default in this template, ITK and VTK must be build separately in order to access and enable those tools. An Open-GL enabled Qt version must be installed previously. After the configuration is done, the project template is build in either Debug or Release configuration. This builds MITK and all its dependencies. In this project, template is not used in the development since we are building our own application outside of the MITK framework, so a new project is started. An helpful guide[1] is available for configuration but some issues may occur that will need closer attention. Is recommended to test the available examples in order to get familar with the toolkit.

## 3.2 Input Images

This thesis worked with the OCT retinal image dataset available from Duke University (Farsiu et al., 2014). This dataset presents images from healthy and patological subjects, as seen in figure 3.2, but on this stage we focus only on healthy retinal images. Volumetric scans (6.7 x 6.7$mm$) were acquired from normal adult subjects using Bioptigen, Inc. SD-OCT imaging systems. The scan is composed by 100 slices. Each slice is a B-Scan and correspond to the $(x, y)$ plane, with a size of 1000 x 512 pixels. The pixel sampling spacing, is 6.7$\mu$m lateral (1000 A-scans) and 67$\mu$m in the azimuthal direction (100 B-scans). The number of A-scans represents the image width.

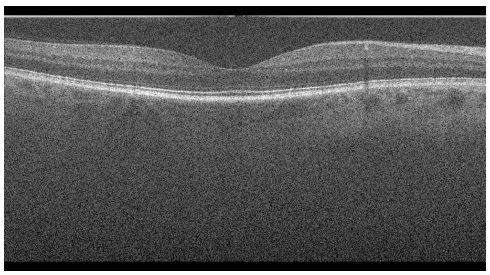

(a) Image of healthy retina

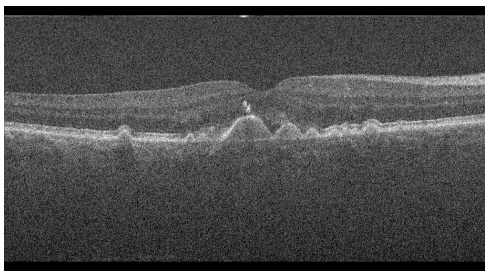

(b) Image of retina with drusen

Figure 3.2: Example images from the used dataset.

[1] $www.mitk.org/wiki/Developer_Tutorial_(Microsoft_Windows)$

## 3.3 Noise Reduction

Before any segmentation there is the need to reduce the speckle noise present in the volume. The figure 3.3 resumes the steps taken. The first one is to extract the volume's region of interest (ROI) in order to remove regions that do not present any useful information. Then the volume is downsampled in a pyramidal approach to half its size. Having considerably reduced the volume size, it is applied an anisotropic diffusion filter to decrease the speckle noise. Lastly, before any further segmentation is important to resample the volume, in order to become isotropic. This sub-chapter explores each step of this process.

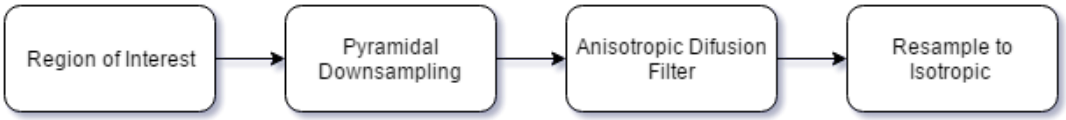


Figure 3.3: Diagram for the noise reduction process.

### 3.3.1 Region of Interest

In order to reduce the computation time it is important to ignore parts of the volume that don't give any relevant information. In the OCT scans, the area above the first layer of the retina and below the last one are useless to the segmentation process and cover a big part of the image. So these areas of the image are cropped, reducing memory usage and computation time. It is important to note that the position of the retina in the OCT scan can change through the 100 B-scans available. To face that, the process starts by projecting the volume into one slice, keeping the maximum pixel value along the several B-scans (figure 3.4(a)). This way it is possible to get the coordinates where there is information across the volume.

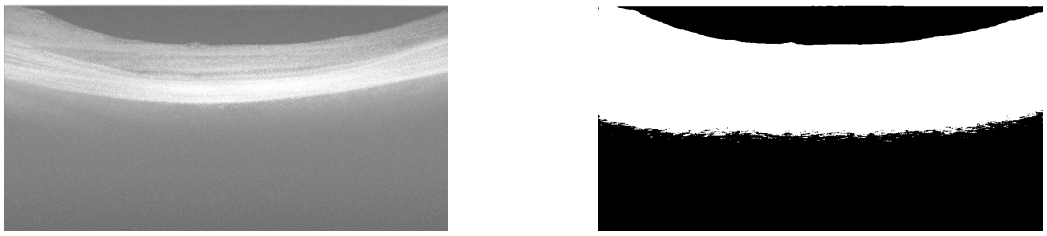

(a) Max. Projection (b) Binarization

Figure 3.4: Process for extracting the ROI

Having one slice with the maximums projection (figure 3.4(b)), a mean filter with a horizontal kernel of 5x1 pixels is applied to remove isolated points away from the ROI, that might be selected by the subsequent binarization, and to fill the gaps inside the ROI. The binarization of the image allows to easily find the top and bottom coordinates of the ROI and select the volume of interest, as shown is figure 3.4(b). It is used a threshold of 140, setting the inside value as white (255) and the outside as black (0). This threshold was determined empirically and shown to be suitable for the data set in study.

The total volume is then cropped in the $y$-axis, keeping the volume in between the two found coordinates (figure 3.5(a)). Cropping the ROI reduces almost to one half of the image size and it will speed up significantly the following noise reduction and segmentation steps.

### 3.3.2 Image Resample

With the objective of reducing memory, computation time and image noise, a downsampling of the image using a pyramidal approach is performed. This method allows the creation of an pyramidal image according to a predefined multi-resolution configuration. This configuration is specified in terms of shrink factors for each multi-resolution level and for each dimension.

A shrink factor of 2 was defined, downsampling the volume to half its size in all dimensions (figure 3.5(b)). To achieve it two computation levels are defined, having the last one a neutral shrink value of 1, demanded by the filter in use. To generate each output image, a Gaussian smoothing is first applied with the variance set to $(shrinkfactor/2)^2$. The smoothed image is then downsampled using the ITK's ResampleImageFilter. This filter resamples an existing image through a identity coordinate transform, interpolating with a linear function. Output information such as spacing, size and direction for the output image should be set. A recursive version of this filter is used since it is about 60% faster than the non-recursive one. This step allows the following anisotropic diffusion filter to perform in reasonable time. The volume should not be downsampled in the $z$-axis since it is already subsampled relative to the $(x, y)$ plane resolution, but without doing it the next step takes more than 4 minutes to perform. In future implementations of the anisotropic diffusion filter in the Graphics Processing Unit (GPU), the z-axis downsampling should not be done.

In fact the dataset used has a different resolution between the $(x, y)$ plane and

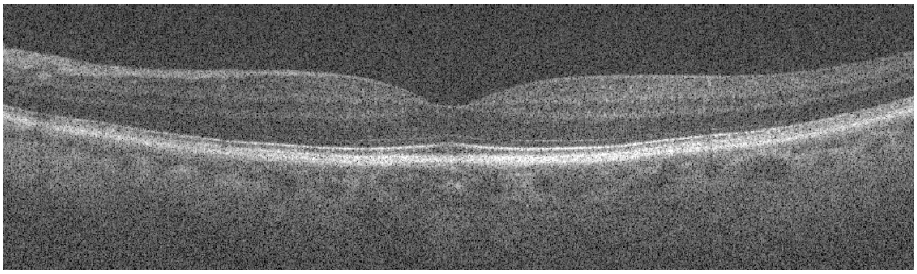

(a) Full size ROI

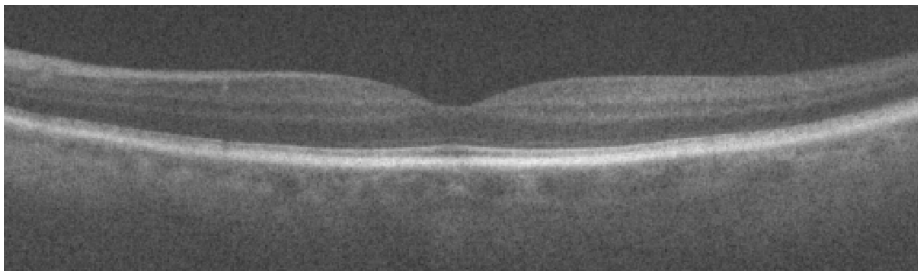

(b) ROI downsample to half of its size

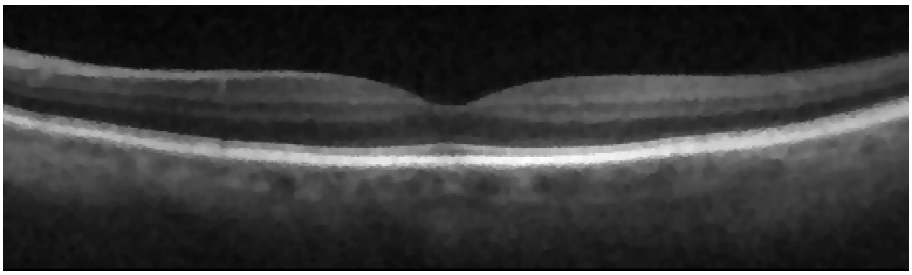

(c) Output of the speckle diffusion filter

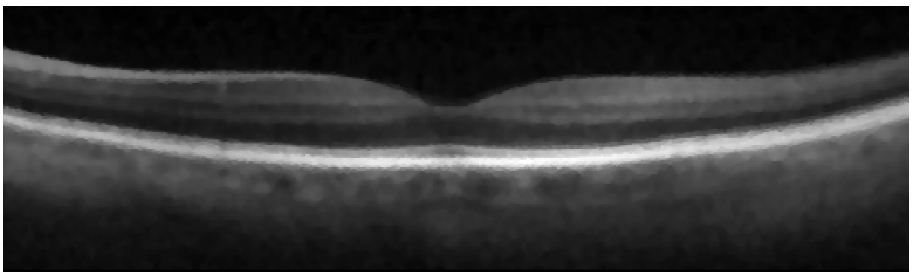

(d) Resampled to be isotropic

Figure 3.5: Example of the noise reduction pipeline.

the $z$-axis with a ratio of 1 to 10. This anisotropy creates distorted rectangular pixels that affect the image processing, since most methods are not ready to deal with this type of anisotropic data. To correct the discrepancy of resolutions the information in the $z$-axis is upsampled, creating virtual slices interpolating the existing ones. The resampled volume has then equal spacing between pixels in all directions, maintaining the physical size of the volume.

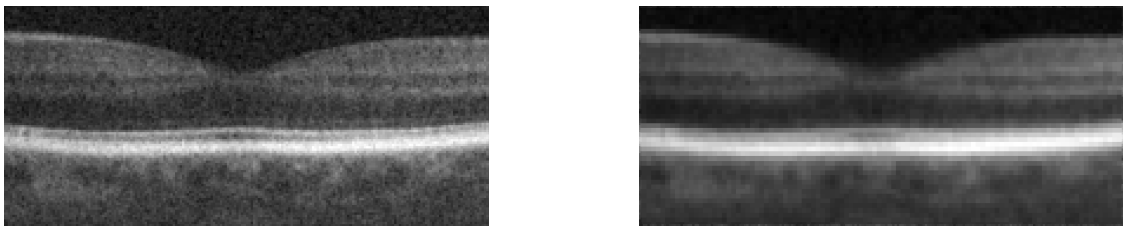

(a) (b)

Figure 3.6: Comparison of an image with different resolutions. Downsampled by a factor of 2 (a) and by a factor of 4 (b)

It was decided to reduce the image by a factor of 2 in the pyramidal downsampling, since a higher reduction would degrade features in the image. A comparison is made in figure 3.6. Decreasing the resolution by a factor of 4 makes the pixels bigger and the segmentation becomes too coarse, with large flat segments that don't give an accurate representation of the original surfaces. However, when resampling the image to become isotropic, the best relation between losing information in the $(x, y)$ plane and the creation of new slices due to interpolation must be found.

To keep the $1000px$ width it will mean to turn each slice into 10. This large interpolation loses image features and results in poor segmentation. Keeping the downsampled width of $500px$ still shows some artifacts in the segmentation and increases the number of pixels 2.5 times, slowing all the process.

A size of $316px$ for the $x$ and $z$-axis was a reasonable solution. It does not increase the total number of pixels and keeps the features of interest (figure 3.5(d). This value is obtained by the geometrical mean between the width and depth of the original volume ($\sqrt{1000 * 100} = 316$). The figure 3.7 compares the sagittal plane before and after upsampling the number of slices

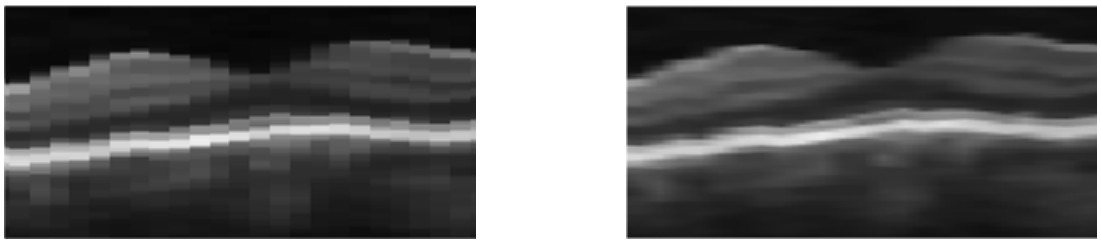

(a) Sagittal plane image detail with original spacing.

(b) Sagittal plane image detail after upsampling

Figure 3.7: Impact of upsampling the number of slices in the volume.

### 3.3.3 Interpolators

The resampling of an image requires interpolation between the points, what can be done using different methods. The chosen interpolation method affects the quality of the resampling and the computation time. More complex interpolation provides better results, with the downside of longer computation times. Hence a balance between time and complexity when choosing the interpolation scheme must be made.

ITK provides nearest neighbor, linear, B-spline and window sinc interpolators (figure 3.8). The most basic one is the nearest neighbor interpolation, which simply uses the intensity of the closest pixels. Linear interpolation assumes a linear intensity variation between image positions and produces a continuous interpolation in space.

When interpolating with B-spline function, coefficients are computed using recursive filtering. A B-spline of order $n$ is a piecewise polynomial function of degree $< n$ in a variable $x$. ITK implementation supports splines of order from 0 to 5.

The windowed sinc interpolation is the best method for discrete data. Based on a Fourier analysis this method delivers the more precise interpolation, convolving the spatial discrete signal with a sinc function. However, it result in long computation times.

The linear interpolator presents the best trade-off between interpolation results and time consumption, and it is suitable for the retinal images in use, being so the chosen method in this work.

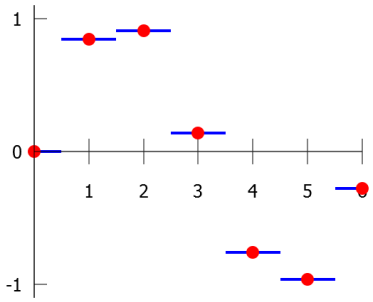


(a) Neares Neighbor (Wikipedia, 2007b)

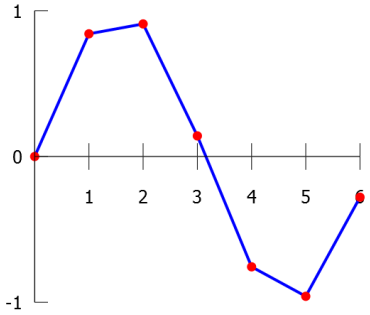


(b) Linear (Wikipedia (2007a))

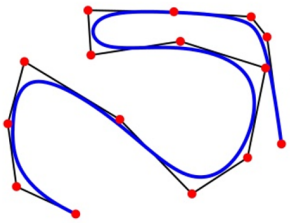

(c) B-spline. Adapted from Technische Universitat München (2010)

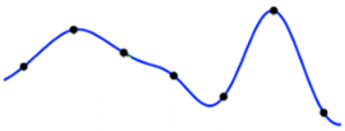

(d) Windowed Sinc. Adapted from Wikipedia (2013)

Figure 3.8: Example of the different interpolation techniques applied to a set of points.

### 3.3.4 Anisotropic Diffusion

OCT images are commonly contaminated with speckle noise. Anisotropic diffusion methods are formulated to reduce noise in images while preserving image edges. A 3D version of the classic Perona and Malik (1990) anisotropic diffusion equation for scalar-valued images was applied in this work.

Two variations of this filter were tested, one using a modified curvature diffusion equation (MCDE) and another using a gradient magnitude based equation, both available in ITK. In figure 3.9 a detail of the same image after the application of both the anisotropic diffusion methods, shows the better edge preservation with the MCDE filter. Both images have been downsampled before.

The result of this filter can be seen in figure 3.5(c) where is clear the impact on speckle noise reduction comparing with the original image.

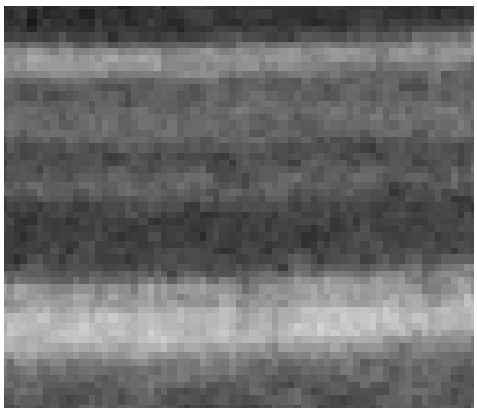

(a) Example of image before filtering

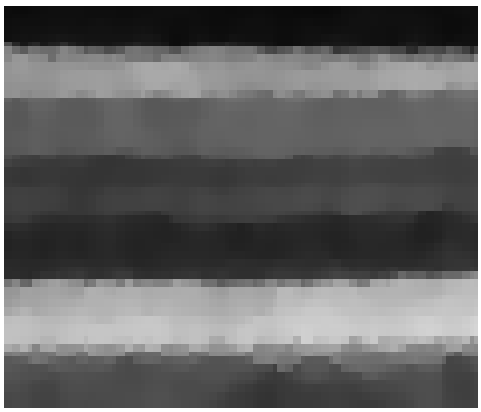

(b) Filtered with MCDE

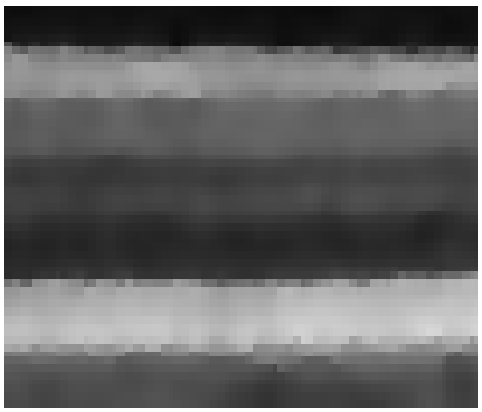

(c) Filtered with Gradient Diffusion

Figure 3.9: Comparison between the two diffusion methods

## 3.4 Segmentation

Being the present thesis a follow up on the work done by Coelho (2015) that uses the Canny filter as main technique for segmentation, here the same method is also used to understand the impact of the volumetric information on its results.

Initially in this work, segmentation was achieved through manipulation of intensities and binarization, but was not suitable for all cases. A graph-cut approach was considered and a basic algorithm was tested, but the complexity of the implementation and the time available to explore it force to abandon the idea.

The segmentation algorithm, shown in figure 3.10 is based on the Canny filter and on locating the surfaces with the help of the input image derivative. It is applied the Canny filter on the resulting image from the noise reduction algorithm. Then the labeling of the individual structures allows to differentiate the top surface from the deeper ones in the retina. To locate the RPE-Choroid surface, the image derivative is used, since the sign of the derivative indicates if a surface is transiting

from a bright to a dark layer or vice-versa. In this case, is known that the RPE-Choroid is a bright to dark transition and so the derivative is negative. In some cases the RPE-Choroid surface is located using a sigmoid filter, presented in section 3.5.2, to enhance the RPE layer and segment it with the Canny filter.

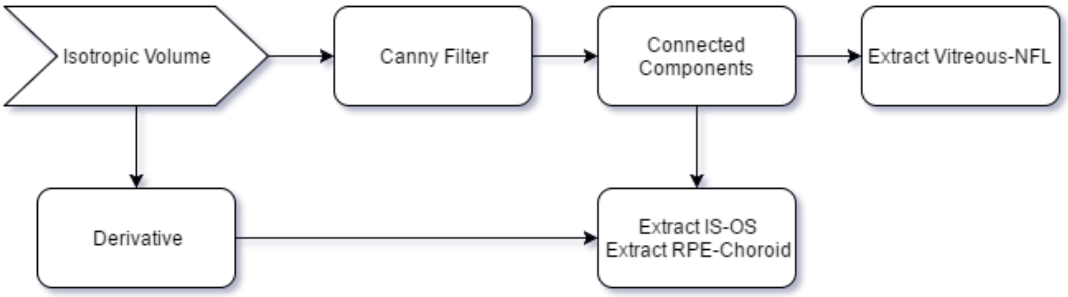


Figure 3.10: Diagram of the process for segmentation of three surfaces of retinal layers .

### 3.4.1 Canny Edge Detection

Canny (1986) defined in his paper three criteria to evaluate the performance of an edge detection filter: good detection, with low probability of marking false edges or failing to mark real edges; good localization, points marked must be close to the center of the real edge and no multiple detection of the same edge. With this definition he developed an optimal layer detection method know by his name. The ITK implementation of this filter for 3D scalar-valued images was used to detect the surfaces between the retinal layers.

The Canny filter is based on the following steps:

1. Smooth the input image with a Gaussian filter;
2. Calculate the second directional derivatives of the smoothed image;
3. Non-Maximum Suppression: the zero-crossings of second derivative are found, and the sign of the third derivative is used to find the correct extrema;
4. The hysteresis thresholding is applied to the gradient magnitude (multiplied with zero-crossings) of the smoothed image to find and link edges. It is recommended a upper to lower ratio between 2:1 to 3:1.

The user is asked to input a desired threshold. That will define the upper threshold and the lower one is set to half of it. By default it was assumed a value of 15. Other parameters that needed to be defined, related to the Gaussian smoothing of the image, namely the variance, set to be the square of the pixel spacing within a slice, and maximum error, that was defined as 0.01.

Before applying the canny filter the image is resized to become isotropic, with the same pixel spacing in all directions. The image to be then processed has a size of 316 x $y$ x 316 pixels, being $y$ dependent of the ROI's height. This is a solution to eliminate the original distance between slices and remove artifacts that result when the slices are not align.

The results from the canny filter can be compared in figure 3.11. Here the original spacing between slices originated an output with thick edges, instead of the expected one pixel wide edge as seen in figure 3.21(b).

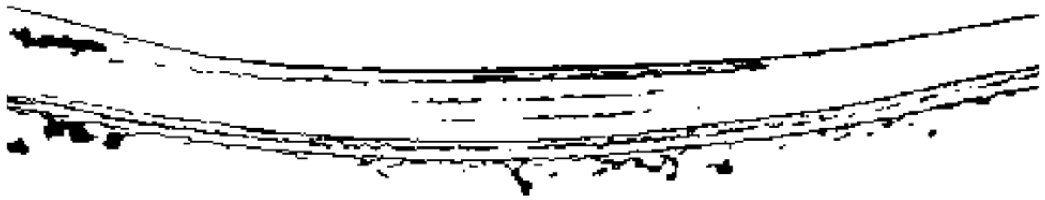

(a) Image $(x, y, z)$ with size 500x117x50 $px$ and spacing of 0.0134, 0.0134 and 0.134 $mm$ respectively.

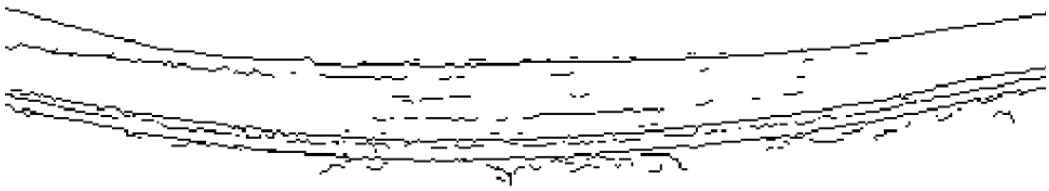

(b) Image $(x, y, z)$ with size 500x117x500 $px$ and spacing of 0.0134 $mm$ in all dimensions.

Figure 3.11: Canny filter's output on anisotropic (a) and isotropic (b) data with same threshold.

Since the segmentation is done in a downsampled isotropic approximation of the original, after the filter it should be resampled to the initial size. Being the output a binary image, aliasing effects appear and the segmentation fails to follow the real edge of the segmented layer. An anti-aliasing filter should be applied before upsampling to maintain the proper segmentation.

Figure 3.12 shows the impact of this filter in the resulting upsampled segmentation. In the section 3.6 more focus is given to aliasing effects.

This upsampling cause a change of the thickness of the segmentation result. It is then necessary to slim it down back to one pixel thickness to allow for a precise location of the surface. This is achieved doing a non-maximum suppression. First a gray scale dilatation is performed using a vertical column with a size of 5 as the kernel (fig. 3.13(b)). The result is then compared back with the original image (fig. 3.13(a)), where only equal pixels, with intensities different from 0 are kept,

(a) Without anti-aliasing filter (b) With anti-aliasing filter

Figure 3.12: Detail of the upsampled segmentation result.

resulting in what is seen in fig. 3.13(c). An average filter is later applied in MATLAB to eliminate the coarse appearance of the segmentation.

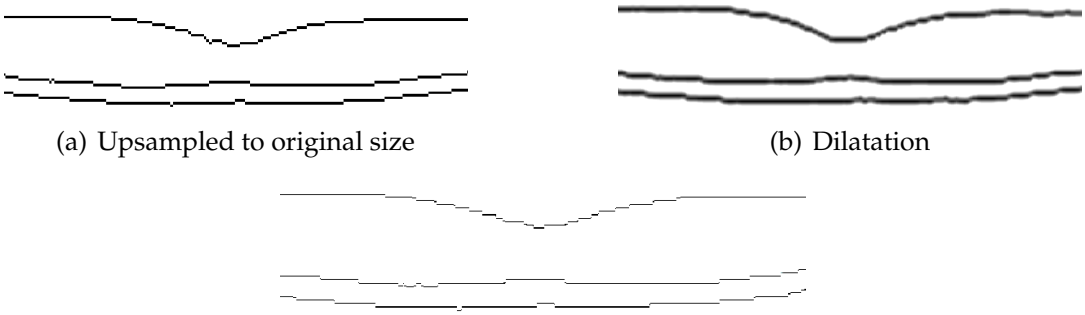

(a) Upsampled to original size (b) Dilatation

(c) Non-maximum suppression

Figure 3.13: Steps to upsampling the segmentation.

### 3.4.2 Volume Division

One of the problems faced when using the canny filter is that the retinal layers do not have a constant intensity and contrast along their $x$-axis, and since canny is dependent on that contrast, it is difficult to find a threshold suitable for all the slice length. Most the times the surface is not detected near the fovea.

Therefore it was decided to divide the volume in different ROIs, where different thresholds could be applied in order to achieve a better layer segmentation. The volume was divided into five regions, being the fovea region isolated in a volume with one third of the length and width of the original one. The canny is then applied to each of the volumes, requiring 5 thresholds to be defined. Being difficult for the user to know the best thresholds, the definition was made automatic using the histogram of the volumes. The thresholds found did not solve the problem in the fovea region, because it is were the vitreous surface is less defined, the RPE shows more intensity, making the threshold too high. The volumes are then merge back together seamlessly to get the original fully segmented with the Canny filter.

To get the correct threshold in each image segment were used the methods available in ITK. Some methods of the presented in Beare (2011) were tested. Figure 3.14 show the thresholds found by the different methods in the same image.

These thresholds ended up not being suitable for the detection of the target surfaces, and so left the choice of the better threshold to the user. The user has no information on how to choose the best threshold value for each of the 5 regions, and setting a value equal for all sections eliminates the purpose of having these regions. It is a better approach to analyze the image layer by layer rather then all at the same time in a smaller region, like what this method tried to achieve.

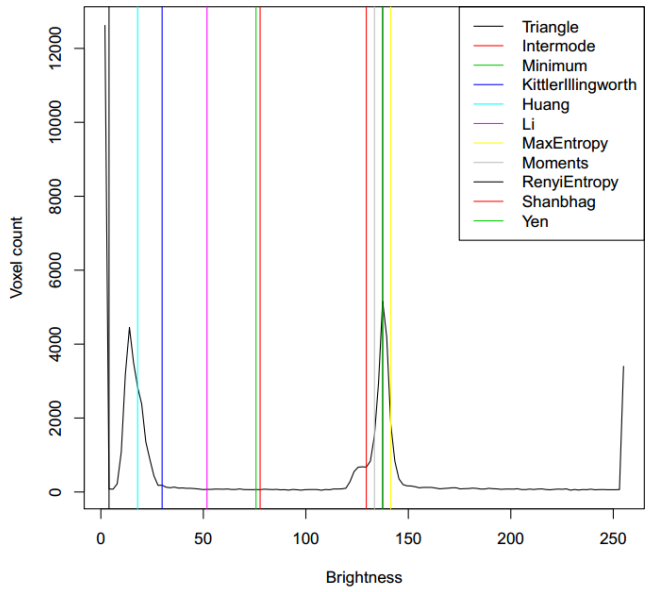


Figure 3.14: Example of an image histogram and thresholds selected by different methods (Beare, 2011).

## 3.5 Other Tools

During the development of the solution, several methods were implemented to gather auxiliary information for the study or just as a experiment to evaluate the output. These are all available in the user interface even though they don't make part of the main pipeline of filters to segment the image.

### 3.5.1 Derivative

The derivative of a image reflects the changes in intensity, and therefore can be used as a tool for edge detection. The sharper the edge (faster transition between different areas) the higher is the value of the derivative. It is directional and presents different outputs for each direction. It is important to distinguish transitions between brighter to darker areas from darker to brighter, being particularly useful to identify the surfaces found in the specific problem of retinal layers segmentation.

The user must specify the direction of the derivative, with respect to the coordinate axis of the image $(x, y, z)$. The order of the derivative, can also be defined. In this case is done the first derivative of the image.

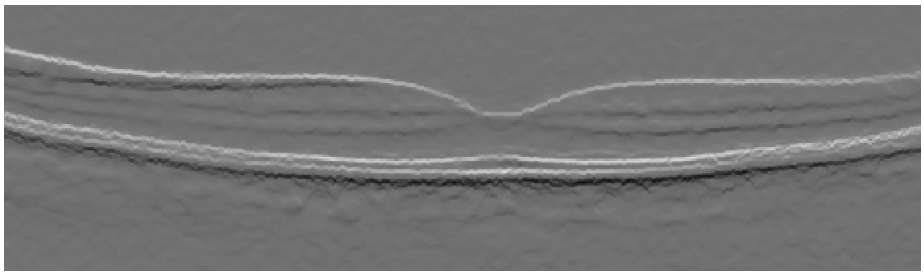

(a) Derivative filter's output in the $y$-axis direction.

### 3.5.2 Sigmoid

In order to change the image contrast, with the objective of enhancing the relevant features a sigmoid filter is applied. This is a s-shaped filter that allows the image contrast to be adjusted with a smoother or sharper effect and to define a threshold from where the intensities are enhanced or faded. The applied transform is given by:

$$f(x) = (Max - Min) \cdot \frac{1}{1 + e^{\frac{-x-\beta}{\alpha}}} + Min. \tag{3.1}$$

The $\alpha$ and $\beta$ parameters are defined by the user and reflect the desired impact of the transformation of the image. The first reflects the sharpness of the filter and the second the threshold. On figure 3.16 are represented the shape of the sigmoid function and its response to different parameters. The default value for $\alpha$ is 10 and for $\beta$ is 190. These will produce an output that enhances the layers from OS to the Choroid (figure 3.15). Another intensity adjustment method used in this work

rescales the values of the voxels in the entire image or in a selected interval to a desired range. Typically it is used after applying a filter to normalize the voxel values along the remaining pipeline and improve visualization. Per example, after the application of the speckle diffusion filter, the region above the vitreous layer presents voxels with a value below 60. In this case the intensities in the interval [60,255] are rescaled to [0,255] and all voxels below 60 are set to zero.

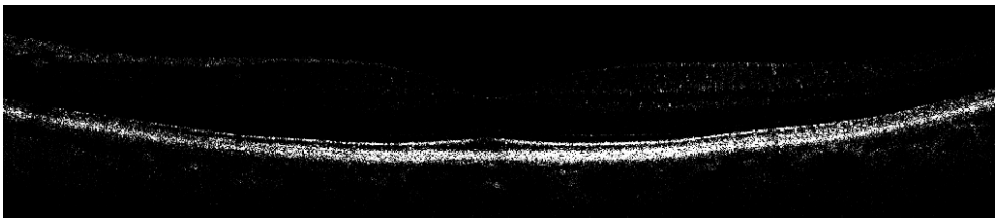

Figure 3.15: Output of the sigmoid filter with $\alpha$ =10 and $\beta$ = 190.

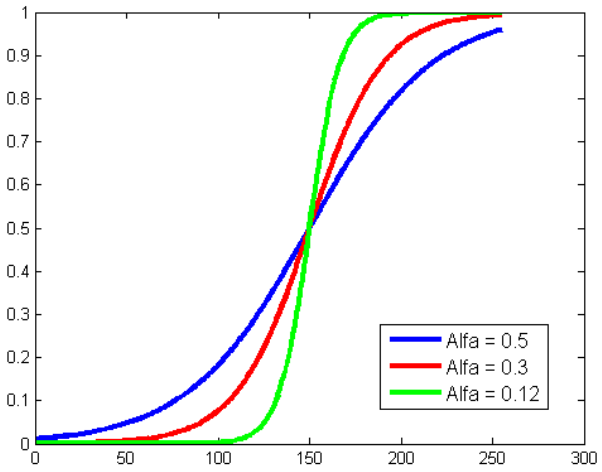


(a) Alpha parameter influence

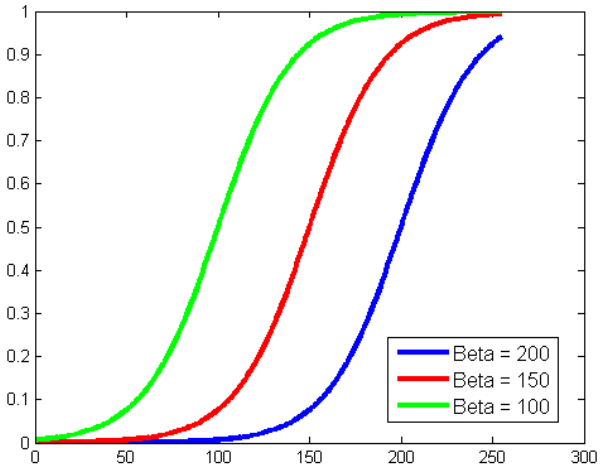


(b) Beta parameter influence

Figure 3.16: Plot of sigmoid function with different parameters

### 3.5.3 Gaussian Filter

A Gaussian filter smooths the image, reducing image noise, and also reducing detail. A recursive implementation available in ITK was used. Here it is applied during the pyramidal downsampling to avoid aliasing artifacts . Figure 3.17 shows the resulting image from this filter.

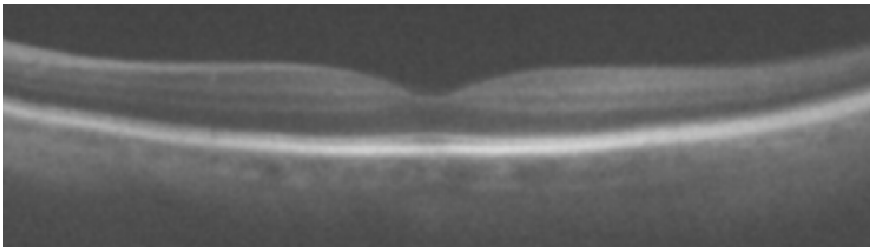

Figure 3.17: Gaussian filter's output with a variance equal to the pixel spacing in all dimensions.

### 3.5.4 Mean and Median filters

The mean and median filters are often used for noise reduction. Both filters generate an image where a given voxel is the mean or median value, respectively, of the voxels in its neighborhood. ITK offers a 3D implementation of these filters, where the neighborhood kernel is a cube with an arbitrary size in each dimension. The median filter preserves the edges of the images, while the mean filter smooths all the image. Figure 3.18 shows the resulting images from these filters. The mean filter smooths the layer limits and so is not suitable as a noise reduction technique in this work. The median filter gives more promising results, but can't keep the same level of detail as the anisotropic diffusion filter.

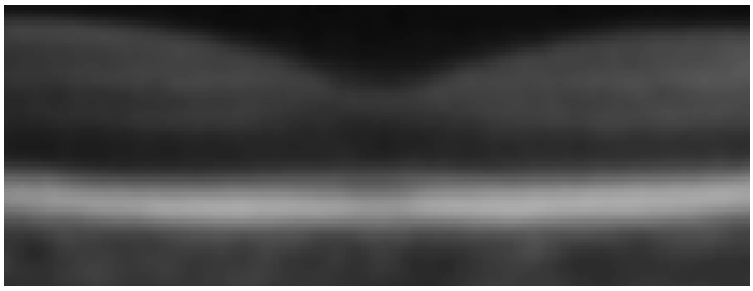

(a) Mean filter's output

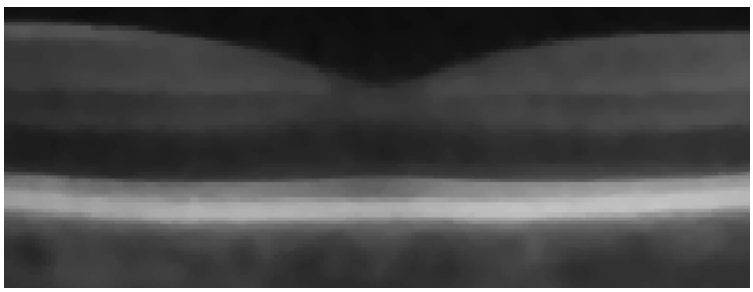

(b) Median filter's output

Figure 3.18: Detail of the result from both filters making five iterations with a kernel of [3x3x3] voxels.

### 3.5.5 Flattening

Flattening the retina image is a method used in some works, and with different motivations. It is used to reduce the total size of the volume (Garvin et al., 2009), to shorten paths in algorithms that use the path weight to perform segmentation (Chiu et al., 2010), or simply to improve visualization of the volume. Here in this work was used to reduce movement artifacts.

Due to eye movements, a change in the overall position of the ROI can be seen between slices. Since the processing of the image is being made in 3D, it will influence the resulting output.

To face this problem the volume will be flatten on the axial direction. This process begins by finding the lower limit of the retina, the surface RPE-Choroid. That will set as the reference. To do this, an intensity transformation is made using the sigmoid filter to enhance the RPE layer, ignoring the remaining part of the image since it as no importance in the flattening process. Then the canny filter is performed to find the desired surface.

The average of the surface height is found in the $z$-axis, to became the new flatten position of the surface. Then subtracting the original position by this value, gives the offset that the surface will have at each point. Finally this offset is applied, resulting in a flatten image in the axial direction.

The full flattening of the image, seen in figure 3.19 is also performed by flattening the in the $x$-axis the reference surface previously found.

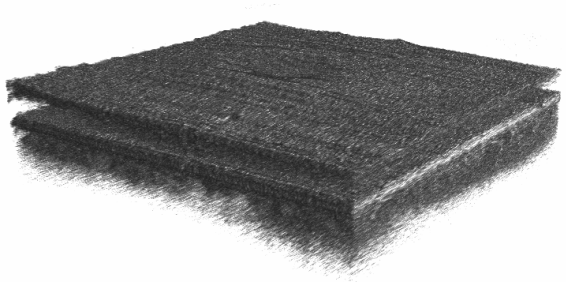

Figure 3.19: Rendering of flatten volume

## 3.6 Visualization

Several volume rendering modes were tested to see which performed better in this particular case of SD-OCT imaging. VTK offers methods for both CPU and GPU.

Besides similar time execution on allocating the image data, it is clear that CPU methods struggle with interaction, like zooming or rotation, being much slower to react, making the software difficult to use. Therefore texture rendering was made in the GPU. Nevertheless the user has the option to choose other techniques like ray casting or MIP, as it can be more suitable for different analysis.

The GPU Ray cast method (figure 3.20(b)) produces a incorrect view of the volume. Its evident that it does not provide the expected results and should be corrected in future versions of the toolkit. This technique implemented in the CPU produces the expected results and the resulting volume is very similar to the obtained from texture mapping, but it is much slower as said before.

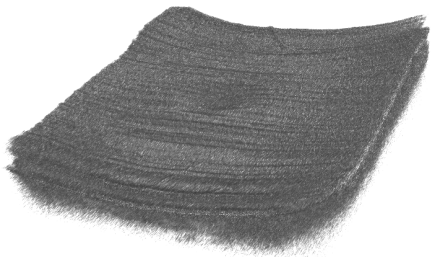

(a) GPU texture

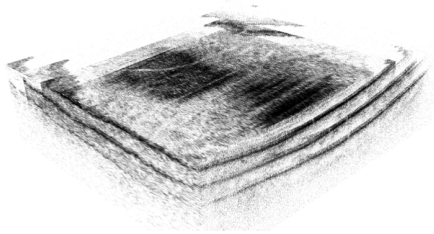

(b) GPU Ray Cast

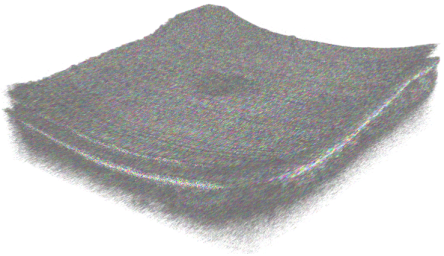

(c) CPU Ray Cast

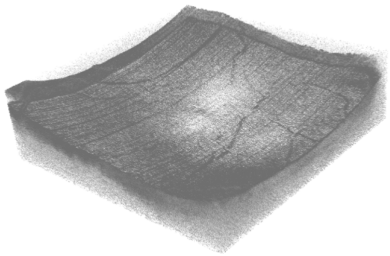

(d) MIP

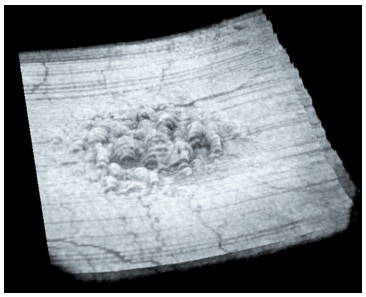

(e) MIP in volume with drusen

Figure 3.20: Different rendering modes

In figure 3.20(d),where the rendering using MIP method is shown, it can be seen as expected the RPE layer of the retina, which is where the voxels have more

intensity, being possible to distinguish the blood vessels on it. Figure 3.20(e) shows the evidence of drusen, using the same method.

The images in figure 3.20 are screen shots from the developed software and were just edited to be clearer when printed. It was opted to maintain a gray value image consistent with the data set, where the opacity values are set by adding control points to the transfer function. In the presented case the points $(100, 0)$, $(200, 0.8)$ and $(255, 1)$ are used. Here the first value in each pair represents the voxel intensity and the second the opacity value valid in [0,1] interval, zero being total transparent and one fully opaque. An interpolation curve is used to define the function between the points.

When rendering the segmentation results, some artifacts can be seen due to the discrete sampling of the image (figure 3.21). Binary volumes, as the ones resulting from segmentation, will show considerable aliasing artifacts when rendered directly. To minimize this effect the anti-aliasing method proposed by Whitaker (2000) is applied.

The user can control the output by setting the RMS value, which must be below 1. The default is 0.07 and will give an acceptable result. The lower the value the tighter is the fitting and so less smoothing is done. This is important not only for better visualization but also to resample a binary image as mention before in the case of the Canny filter result.

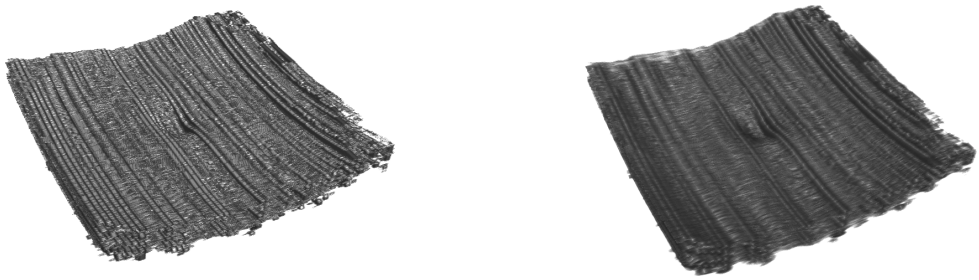

(a) (b)

Figure 3.21: Rendering of Canny filter's output without flattening. Original (a) and after application of the anti-aliasing filter (b) with RMS of 0.07.

## 3.7 Prototype

The software is organized in two classes, *MainWindow* that holds all the graphic interface and the input and output of data and *SegmentationWindow* is where all filters implemented for noise reduction and segmentation are.

MITK is used to load images and to convert between MITK and ITK formats. Also, it provides the widgets that allow the visualization and interaction with the images. The VTK is used indirectly through MITK in the rendering process. The graphic elements, like buttons, sliders, labels are provided by Qt.

ITK provides the functions responsible for the 3D image processing. All the methods implemented support multi-threading. Some effort to implement methods that support parallel processing in the GPU were made, although the solution couldn't build successfully, likely due to incompatibility with the hardware used since it was not present in the short list of tested systems.

In figure 3.22, is presented the interface, that allows the user to manipulate the images and interact with them.

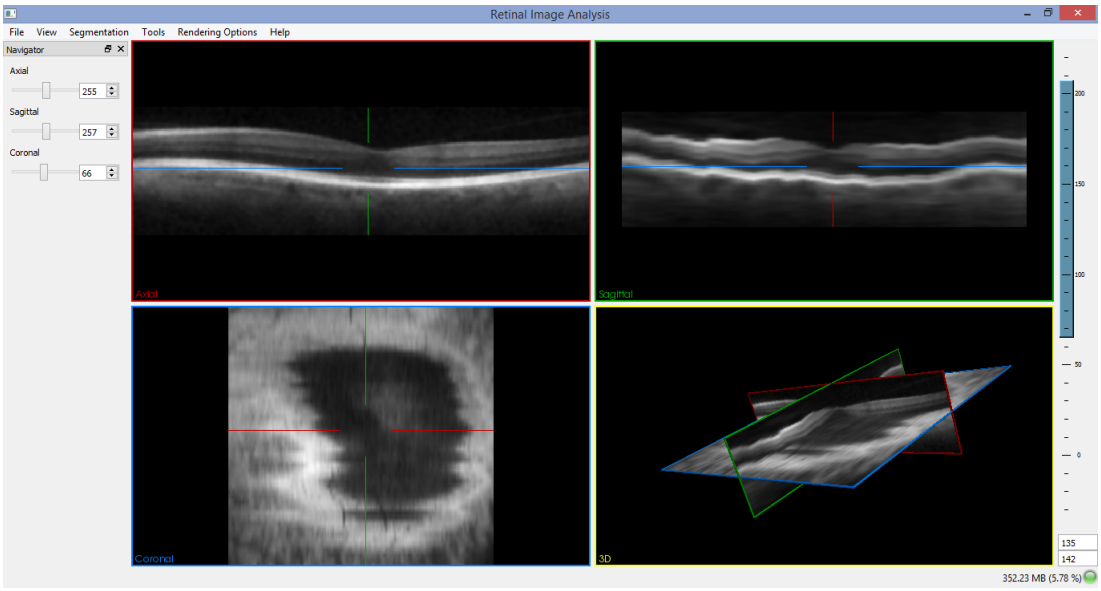


Figure 3.22: Graphic User Interface

The user is asked to give an input image. Many different formats can be open by the software, but for 3D viewing are expected files in DICOM or NRRD format.

The volumetric image is usually presented in four panels, three with 2D view of the volume in axial, sagittal and coronal perspectives, and the last one with a 3D plane widget or, when enabled, the 3D rendering of the volume. Inside each display panel there is a crosshair that represents the relative position of the

different perspectives, facilitating the navigation. Also, on the upper right corner the user can access more options to customize the view and even change the layout. The panels can be maximized inside the main view and their placement, as well as the number of panels can be changed in various ways.

This panels are the main point of interaction with the image. It allows the user to:

- Scroll - scrolls through slices using the mouse wheel;
- Zoom - pressing the right button and moving the cursor up or down;
- Move crosshair - pressing the left button and moving the cursor;
- Move the image - press the mouse wheel and dragging the image;

On the right side of the window there is a vertical bar to control brightness and contrast. By moving its position and adjusting its size is possible to improve the data visualization. With a right-click on top of it, more options are shown, such as auto adjust of the window.

Docked in the left side of the window are navigation controls that display the current slice in all the views and give the user a alternative way to interact with the volume through the use of sliders. By selecting the slider the user can go across the slices using the keyboard's arrows.

On the bottom of the window there is a task bar that shows a short description of the function being selected. Also on the right end of the bar, memory usage of the program is shown.

In the menu bar there are the following menus: File, View, Segmentation, Tools Rendering Options and Help. In the *File* menu the user can open and save a file and close the application.

On the *View* menu is possible to enable/disable the 3D rendering of the volume by checking the *View 3D* button. The user can also enable/disable the *Texture Interpolation* which blurs the edges between image pixels, smoothing the segmentation result shown. In the option *All Layers*, the full pipeline for segmentation is performed and all the resulting surfaces are shown overlapping the input image.

The *Segmentation* menu holds all the noise reduction and segmentation functions:

- *Get ROI*: Extracts the region of interest;
- *Pyrdown Resampler*: Resamples the volume to half is size in every direction. Extracts the ROI if not done previously;
- *Resample to Isotropic*: resamples the image to be isotropic with a defined spacing of $0.021mm$.

- *Resample to Original*: resamples the image to the original size of the ROI.
- *Resample to Anisotropic*: Resamples the image back to the 1 to 10 ratio between in-plane $(x, y)$ and inter-plane resolution, maintaining the slice size.
- *Speckle Reduction*: Applies the anisotropic diffusion filter for noise reduction. Extracts the ROI and resamples the volume if not done before.
- *Canny Filter*: Applies the Canny filter on the current image. Asks for desired threshold.
- *Label Surface*: Apply a connected components method to label the different surfaces found.
- *Align Slices*: Align all the slices by the RPE-Choroid surface. A flattening of the sagittal plane is achieved;
- *Align Volume*: Flattens the entire volume. The options *Get Vitreous*, *Get IS-OS* and *Get Choroid-RPE* perform the segmentation of the respective surfaces.

In the menu *Tools* it is given access to some filters. Each option applies the named filter in the current image and asks for input when needed. The filters available are the *Binarization*, *Sigmoid*, *Derivative*, *Gaussian*, *Gradient*, *Mean*, *Median* and *Anti-aliasing*. The option *Back* gets the image previous to the application of any filter. The *Intensity Rescale* changes the intensity values of the image for a defined interval.

On the *Rendering Options* menu is possible to define rendering preferences:

- *Ray Cast Rendering*: Selects Ray Cast as rendering method to be performed. This method is rendered in the CPU;
- *MIP Rendering*: Selects Maximum Intensity Projection as rendering method to be performed, also rendered in the CPU.
- *GPU Rendering*: Selects texture interpolation as rendering method. As the name states this method renders the volume in the GPU;
- *White Background*: This option simple changes the background color of the last panel, where the 3D rendering is shown. When selected the background is white, otherwise the background is black. It aims to help visualization when acquiring screen shots of the image.

CHAPTER 4

# RESULTS

## 4.1 Input Images

Assembled in MATLAB format, the dataset consists of 38400 B-scans from 269 AMD patients and 115 normal subjects, and presents the manual segmentation boundaries on a 5mm diameter centered in the fovea. The manual segmentation was made by two certified OCT readers from Duke Reading Center.

All the scans were converted from MATLAB to DICOM format. This format stores the 2D images in separate files, all numerically sorted in a folder. However during the thesis development it was found to be easier to manipulate data in NRRD format, as it stores the whole volume in one single file, and the toolkit has better support for writing in this format.

The results are compared with the manual segmentation available in the dataset. The information on the segmented surfaces position is exported to a Comma-Separated Values (CSV) file, and the comparison and evaluation is made in MATLAB, because it is the original format of the dataset, and therefore easier to manipulate.

Seven different volumes from normal subjects, with 100 images each, were used to compare the results. The 20 first and 20 last images from each set are ignored, as well as the 100 first and last columns from each image, since the OCT scan presents low quality in these areas and no data is available to compare. A total of 420 B-Scans were analyzed.

## 4.2 Validation of Results

The validation of the results achieved through the proposed method was made by comparing the thickness of the layers delimited by two detected surfaces with the manual segmentation on 2D images of the same dataset.

It is used the thickness so that the results are independent of the position of the surfaces, since the segmentation from an 3D output might not present the same spacial location as in the 2D segmentation. This is visible when there are sudden changes in the overall position of the retina between slices in the OCT volume.

The mean error between the thickness of the layers was calculated and its analysis shows if the solution produces acceptable results. A reasonable result should be equal or lower than the error found when comparing the segmentation done by different specialists on the same image.

Chiu et al. (2010) presents the mean error from the manual segmentation done by 2 specialist, used to validate their own method. They developed a MATLAB based software called Duke OCT Retinal Analysis Program (DOCTRAP) which results are present in table 4.1. Since it works with the same dataset, the results from this software will be compared with the ones from the current proposal.

Table 4.1: Mean Error (pixels) between the layer's thickness

| **Layers** | **Manual** | **DOCTRAP** | **Chiu2012b** | **Proposed** |
|---|---|---|---|---|
| Total retina | $2.22 \pm 1.0$ | $0.94 \pm 0.82$ | $1.29 \pm 0.86$ | $3.72 \pm 0.3$ |
| IS-RPE | – | – | $0.98 \pm 0.82$ | – |
| IS-Choroid | – | – | – | $13.18 \pm 0.34$ |

To be noted, the manual segmentation shows the marking of the OS-RPE surface, while the proposed method segments the ONL-IS surface. The thickness of the retina between the ONL-IS and the RPE-Choroid surfaces is compared with the thickness from IS-OS to RPE-Choroid surfaces, the manually segmented in the dataset. Therefor the high error presented includes the expected thickness differences between the segmented layers. As the surfaces can be considered approximately parallel, the standard deviation of the error may reflect the correctness of the segmentation. Each pixel corresponds to $3.23\mu$m.

Figure 4.1 shows the resulting segmentation on the downsampled image. After, the segmented layers are upsampled to the original size of the ROI in order to be overlap the original image, as seen in figure 4.2. This data is then exported to MATLAB to proceed with the comparison with the manual segmentation available.

Before any calculations a smoothing filter is applied to the segmentation data as a last step in the segmentation of the layers. The result can be seen in figure 4.2(a), where the segmentation is better fitted to the OCT image.

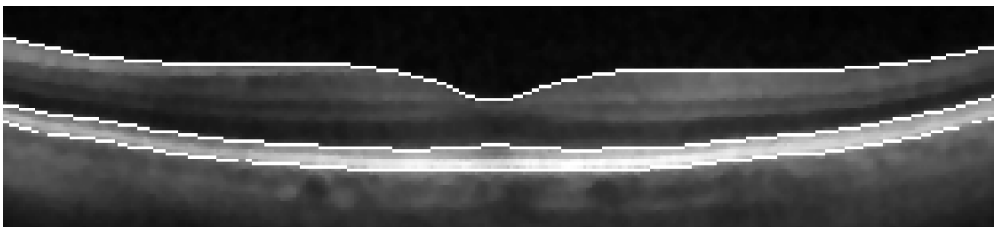

(a) Axial plane

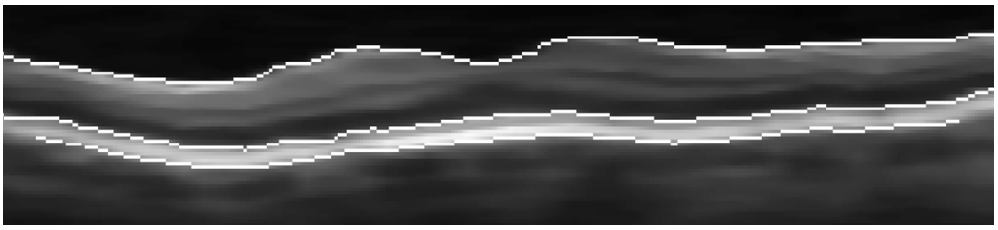

(b) Sagittal plane

Figure 4.1: Segmentation of the three target surfaces on resampled volume with a size of [315x90x308] pixels. From top to bottom: Vitreous-NFL, IS-OS and RPE-Choroid.

The results are not as good as expected since the mean error between the layers thickness is larger than the error found between two specialists.

In this solution no adjustments or learning algorithms were implemented to better match the automatic to the manual markings done by experts.

In the other results present in table 4.1 however, the results were further processed to close the gap between automatic and manual segmentation. The mean error for the present solution is calculated using a larger set of images than any other method on the table. Also all the methods in the comparison use 2D techniques in their segmentation. The impact of 3D information on the segmentation also reflects in the comparative results. Having in consideration the neighbor slices, the segmentation of one feature will not perfectly match the equivalent in a 2D approach, due to interpolation between consequent slices.

One problem with the medical imaging systems is the different acquisition resolutions in each direction, being usually much lower in the $z$-axis. The used data set does not present a truly 3D image, but rather a set of 2D image with regular spacing between them that allows an approximation to the correspondent volume. This brings the need to resample the images in order to achieve an isotropic volume

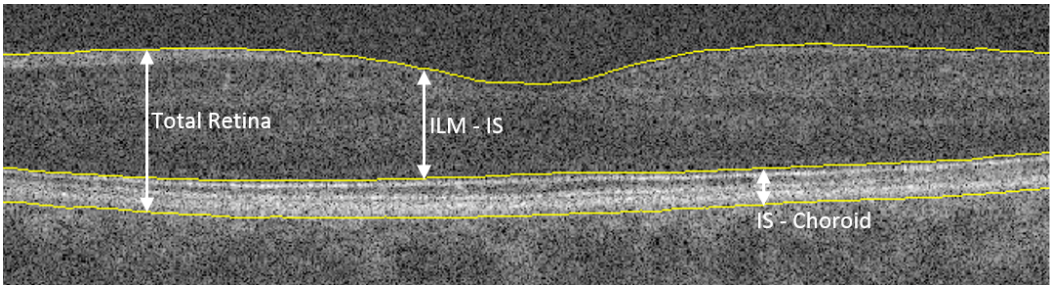


(a) Resulting segmentation

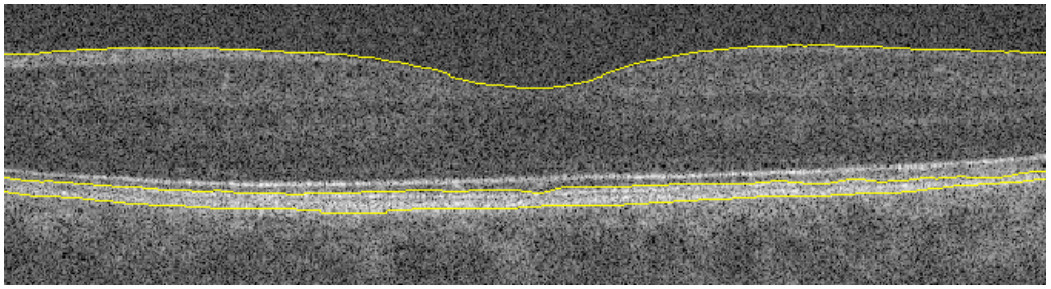

(b) Manual Segmentation

Figure 4.2: Final segmentation after resampling to original size of the ROI and smoothing the output.

where regular filtering can be applied. As a result of such resampling, the image loses some of its original information and this is one of the causes for the results to not better match other solutions. Even though the acquisition methods should aim to reduce this problem, downsampling the image is still a step made in most of the solutions to reduce the computational needs, not fully taking advantage of the large resolutions available.

## 4.3 Performance

As expected in large image sets, the computational needs are quite high. This often means a long computation time relative to what a user would expected from an software interface.

Manual segmentation took an average time of 3.5 minutes per slice (Chiu et al., 2012) and the solution from Coelho (2015) also based in the Canny filter takes 9 seconds per slice, what for a volume with 100 slices represents 15 minutes per volume, which is around the same time as the proposed method, depending on the ROI's size of each set. This is running in a Windows 8.1, 64-bit machine,

with the Intel Core i7-2630QM processor at 2.00GHz, 6Gb of RAM and an AMD Radeon HD 6700M graphic card.

CHAPTER 5

# CONCLUSION

The present work aims to develop tools for processing and visualization of 3D retinal SD-OCT images, in order to segment the retinal layers.

During the development of this study many challenges were faced. When starting the implementation, the aim to use C# language lead to the use of wrappers of the most recognized toolkit for 3D image processing. This ended up making difficult the task to use the already complex toolkit. The solution was found in MITK, using C++ and having a framework that fully integrated the toolkits needed for both 3D image processing and visualization, the ITK and VTK respectively.

The visualization of 3D images is achieved through an user interface that enables the application of different rendering techniques on the OCT scan images. The user can then freely interact with the image and view each slice in the axial, sagittal and coronal planes. This gives a better view of the overall subject and can be important in the diagnosis and detection of anomalies. The use of some filters is also available to the user to improve the analysis of the retinal features, like noise reduction, cropping, resampling, intensity rescale and segmentation filters.

Being the noise of the image, namely the speckle noise, one characteristic always present, was important to deal with it without destroying any important features on the image. The curvature anisotropic diffusion filter revealed to be a good solution on removing noise and preserving the edges of the layers of the retina. The size of the volumetric images implied long computational times. There is the need to downsample the images in order to produce results in a reasonable time. This step also has a positive impact in noise reduction.

Implementation of parallel processing techniques will allow to explore the full resolutions that are available without major setbacks. Although the long processing times, comparing with a manual segmentation and other 2D methods, the time consumption of solution presented is acceptable.

The segmentation of retinal layers did not achieve the expected results. After pre-processing and resampling the image, the Canny filter is applied to detect the features of interest that are later extracted. By comparing the retinal layer's thickness from manual and automatic segmentation, the mean error and standard deviation are calculated. The resulting error is greater than the error between different manual segmentation and so does not meet the aimed precision for the solution. Still using a 3D implementation of the Canny filter is a suitable approach for this segmentation problem, although difficulties were found dealing with the difference between lateral and azimuthal resolutions.

Recent techniques like graph-cuts, have shown good results in the segmentation of volumetric OCT images and avoid dealing with some characteristic problems like the presence of noise.

In comparison with other 2D solutions, besides the advantage of allowing a 3D visualization of the SD-OCT scan, and look through the data from three different perspectives, this solution makes usage of the extra dimension a volumetric image brings. Not only the segmentation combines neighbor slices of the volume but also the image processing uses a cubic kernel in opposite of the classic square in two dimensions, therefor each calculation has more information available to achieve accurate results.

The developed prototype and tools can be used to further develop the segmentation in other medical subjects. It presents a platform for teaching and investigation on 3D image analysis, since it gives the user a good interface, with a set of filters to manipulate volumetric images and the source code to improve on the present solution and implementation.

## 5.1 Future Work

Being this a first step in 3D image processing, some follow up work and improvements can take place. The produced prototype is available for download with all the source code[1]. This will help to jump start future work as a better knowledge on

[1] https://goo.gl/YXdejM

the implementation of the toolkit filters and Qt interface is now at one's disposal. There is a lot to explore inside ITK, VTK and MITK itself. Studying these toolkits showed how a powerful tool they can be in image processing and visualization.

Not much attention was given to optimize the code. Further improvement on this will contribute to reduce segmentation time. The perspective of implementing some filters on GPU made the code optimization not a priority issue in this work, since GPU processing will reduce the computation time. The toolkits already offer same basic classes to allow this and some are ready to use 3D filters like the average filter. The interface can also improve with more feedback to the user.

Finally the segmentation and extraction of features from the retinal layers should be further explored in order to achieve a better result in comparison with manual segmentation and improve the robustness of the method. The extraction of more layers and detection of anomalies in the retina, as drusen for instance, should be the objective of consequent work.

# BIBLIOGRAPHY


Anatomia Online (2014). *Introdução ao Estudo da Anatomia*. URL: http://anatomiaonline.com/introducao/generalidades.html (visited on 2016-03-22).

Avanaki, M. R. N., R. Cernat, P. J. Tadrous, T. Tatla, A. G. Podoleanu, and S. Ali Hojjatoleslami (2013). "Spatial compounding algorithm for speckle reduction of dynamic focus OCT images". *IEEE Photonics Technology Letters* 25(15), pp. 1439–1442. ISSN: 10411135. DOI: 10.1109/LPT.2013.2266660.

Baghaie, A., M. D. Roshan, and Z. Yu (2014). "State-of-the-Art in Retinal Optical Coherence Tomography Image Analysis". *Quantitative Imaging in Medicine and Surgery* 5(4), pp. 1–18. DOI: 10.3978/j.issn.2223-4292.2015.07.02.

Beare, R. (2011). "Histogram-based thresholding - some missing methods". *The Insight Journal*, pp. 49–56.

Bristol University (2000). *Structure of the Retina*. URL: http://137.222.110.150/calnet/visual2/page2.htm (visited on 2016-03-07).

Canny, J. (1986). "A Computational Approach to Edge Detection". *IEEE Transactions on Pattern Analysis and Machine Intelligence* PAMI-8(6), pp. 679–698. DOI: 10.1109/TPAMI.1986.4767851.

Chiu, S. J., X. T. Li, P. Nicholas, C. a. Toth, J. a. Izatt, and S. Farsiu (2010). "Automatic segmentation of seven retinal layers in SDOCT images congruent with expert manual segmentation." *Optics express* 18(18), pp. 19413–19428. ISSN: 1094-4087. DOI: 10.1364/OE.18.019413.

Chiu, S. J., J. A. Izatt, R. V. O'Connell, K. P. Winter, C. A. Toth, and S. Farsiu (2012). "Validated automatic segmentation of AMD pathology including drusen and geographic atrophy in SD-OCT images." *Investigative ophthalmology & visual science* 53(1), pp. 53–61. ISSN: 1552-5783. DOI: 10.1167/iovs.11-7640.

Coelho, M. (2015). "Segmentação de camadas retinianas em imagens SD-OCT (RELY)". MA thesis. Universidade Nova de Lisboa.

Farsiu, S., S. J. Chiu, R. V. O'Connell, F. a. Folgar, E. Yuan, J. a. Izatt, and C. a. Toth (2014). "Quantitative classification of eyes with and without intermediate age-related macular degeneration using optical coherence tomography." *Ophthalmology* 121, pp. 162–72. ISSN: 1549-4713. DOI: 10.1016/j.ophtha.2013.07.013.

Garvin, M. K., M. D. Abràmoff, R. Kardon, S. R. Russell, X. Wu, and M. Sonka (2008). "Intraretinal layer segmentation of macular optical coherence tomography images using optimal 3-D graph search". *IEEE Transactions on Medical Imaging* 27(10), pp. 1495–1505. ISSN: 02780062. DOI: 10.1109/TMI.2008.923966.

Garvin, M. K., M. D. Abràmoff, X. Wu, S. R. Russell, T. L. Burns, and M. Sonka (2009). "Automated 3-D intraretinal layer segmentation of macular spectral-domain optical coherence tomography images." *IEEE transactions on medical imaging* 28(9), pp. 1436–1447. ISSN: 0278-0062. DOI: 10.1109/TMI.2009.2016958.

Gilboa, G., N. Sochen, and Y. Y. Zeevi (2004). "Image enhancement and denoising by complex diffusion processes." *IEEE transactions on pattern analysis and machine intelligence* 26(8), pp. 1020–36. ISSN: 0162-8828. DOI: 10.1109/TPAMI.2004.47.

Heidelberg Engineering (2016). *Spectral Domain Optical Coherence Tomography (SD-OCT)*. URL: http://www.heidelbergengineering.com/us/products/spectralis-models/technology/spectral-domain-oct/ (visited on 2016-01-20).

Johnson, H. J. and M. M. Mccormick (2014). "The ITK Software Guide Book 1 : Introduction and Development Guidelines".

Kafieh, R., H. Rabbani, and S. Kermani (2013a). "A Review of Algorithms for Segmentation of Optical Coherence Tomography from Retina". *Journal of medical signals and sensors* 3(1), pp. 45–60.

Kafieh, R., H. Rabbani, M. D. Abramoff, and M. Sonka (2013b). "Intra-retinal layer segmentation of 3D optical coherence tomography using coarse grained diffusion map". *Medical Image Analysis* 17(8), pp. 907–928. DOI: 10.1016/j.media.2013.05.006.

Kennedy, B. F., T. R. Hillman, A. Curatolo, and D. D. Sampson (2010). "Speckle reduction in optical coherence tomography by strain compounding". *Optics letters* 35(14), pp. 2445–2447. DOI: 10.1364/OL.35.002445.

Kitware (2016). *VTK*. URL: http://www.vtk.org/ (visited on 2016-02-08).

Kraus, M. F. et al. (1991). "Motion correction in optical coherence tomography volumes on a per A-scan basis using orthogonal scan patterns". *Science Commun. Biomedical Optics Express* 254(6), pp. 1178–1181.

Lacroute, P. and M. Levoy (1994). "Fast volume rendering using a shear-warp factorization of the viewing transformation". *Proceedings of the 21st annual conference on Computer graphics and interactive techniques - SIGGRAPH '94*, pp. 451–458. ISSN: 0167-7055. DOI: 10.1145/192161.192283.

Levoy, M. (1988). "Display of surfaces from volume data". *IEEE Computer Graphics and Applications* 8(3), pp. 29–37. ISSN: 0272-1716. DOI: 10.1109/38.511.

Li, K., X. Wu, D. Z. Chen, and M. Sonka (2006). "Optimal surface segmentation in volumetric images - A graph-theoretic approach". *IEEE Transactions on Pattern Analysis and Machine Intelligence* 28(1), pp. 119–134. ISSN: 01628828. DOI: 10.1109/TPAMI.2006.19.

Lorensen, W. E. and H. E. Cline (1987). "Marching cubes: A high resolution 3D surface construction algorithm". *Computer Graphics* 21(4), pp. 163–169. ISSN: 00978930. DOI: 10.1145/37402.37422.

MITK (2016). *The Medical Imaging Interaction Toolkit (MITK)*. URL: http://mitk.org/wiki/MITK (visited on 2016-01-15).

Mora, A. D., P. M. Vieira, A. Manivannan, and J. M. Fonseca (2011). "Automated drusen detection in retinal images using analytical modelling algorithms". *BioMedical Engineering OnLine* 10(1), pp. 1–16. ISSN: 1475-925X. DOI: 10.1186/1475-925X-10-59. URL: http://dx.doi.org/10.1186/1475-925X-10-59.

NEMA (2016). *DICOM: About DICOM*. URL: http://dicom.nema.org/Dicom/about-DICOM.html (visited on 2016-02-03).

Niemeijer, M., M. K. Garvin, B. van Ginneken, M. Sonka, and M. D. Abràmoff (2008). "Vessel Segmentation in 3D Spectral OCT Scans of the Retina". *Proc. SPIE 6914, Medical Imaging 2008: Image Processing* 6914. ISSN: 0277786X. DOI: 10.1117/12.772680.

NRRD (2016). *nrrd*. URL: http://teem.sourceforge.net/nrrd (visited on 2016-02-03).

Pal, N. R. and S. K. Pal (1993). "A review on image segmentation techniques". *Pattern Recognition* 26(9), pp. 1277–1294. ISSN: 00313203. DOI: 10.1016/0031-3203(93)90135-J.

Papademetris, X. and A. Joshi (2009). "An Introduction to Programming for Medical Image Analysis with the Visualization Toolkit". *Yale University*.

Perona, P. and J. Malik (1990). "Scale-space and edge detection using anisotropic diffusion". *IEEE Transactions on Pattern Analysis and Machine Intelligence* 12(7), pp. 629–639.

Pham, D. L., C. Xu, and J. L. Prince (2000). "Current Methods in Medical Image Segmentation".

Pircher, M., E. Gotzinger, R. Leitgeb, A. F. Fercher, and C. K. Hitzenberger (2003). "Speckle reduction in optical coherence tomography by frequency compounding". *Journal of Biomedical Optics* 8(3), p. 565. ISSN: 10833668. DOI: 10.1117/1.1578087.

Qt (2015). *About Qt*. URL: http://wiki.qt.io/About_Qt (visited on 2016-01-19).

Salinas, H. M. and D. C. Fernández (2007). "Comparison of PDE-based nonlinear diffusion approaches for image enhancement and denoising in optical coherence tomography". *IEEE Transactions on Medical Imaging* 26(6), pp. 761–771. ISSN: 02780062. DOI: 10.1109/TMI.2006.887375.

Schmitt, J. M. (1997). "Array detection for speckle reduction in optical coherence microscopy." *Physics in medicine and biology* 42(7), pp. 1427–39. ISSN: 0031-9155.

Schmitt, J. M., S. H. Xiang, and K. M. Yung (1999). "Speckle in Optical Coherence Tomography". *J. Biomed. Opt.* 4, pp. 95–105.

Smith, R. T., J. K. Chan, T. Nagasaki, U. F. Ahmad, I. Barbazetto, J. Sparrow, M. Figueroa, and J. Merriam (2005). "Automated Detection of Macular Drusen Using Geometric Background Leveling and Threshold Selection". *Archives of ophthalmology* 123(2), pp. 200–206. ISSN: 0003-9950. DOI: 10.1001/archopht.123.2.200.

Srinivasan, P. P., S. J. Heflin, J. a. Izatt, V. Y. Arshavsky, and S. Farsiu (2014). "Automatic segmentation of up to ten layer boundaries in SD-OCT images of the mouse retina with and without missing layers due to pathology". *Biomedical Optics Express* 5(2), pp. 348–65. ISSN: 2156-7085. DOI: 10.1364/BOE.5.000348.

Sun, Y. and T. Zhang (2012). "A 3D Segmentation Method for Retinal Optical Coherence Tomography Volume Data".

Technische Universitat München (2010). *B-Spline Curve*. URL: http://m2matlabdb.ma.tum.de/download.jsp?MC{_}ID=7{\&}SC{_}ID=7{\&}MP{_}ID=485 (visited on 2016-03-18).

Wasatch Photonics (2015). *OCT Fundamentals*. URL: http://wasatchphotonics.com/oct-tutorial/ (visited on 2015-12-10).

Westover, L. (1990). "Footprint Evaluation for Volume Rendering". ˜ *Computer Graphics* 24(4).

Whitaker, R. T. (2000). "Reducing aliasing artifacts in iso-surfaces of binary volumes". *Proceedings of the 2000 IEEE symposium on Volume visualization - VVS '00*, pp. 23–32. DOI: 10.1145/353888.353893.

Whitaker, R. T. and X. Xue (2001). "Variable-conductance, level-set curvature for image denoising". In: *Proceedings 2001 International Conference on Image Processing (Cat. No.01CH37205)*. Vol. 2, pp. 142–145. ISBN: 0-7803-6725-1. DOI: 10.1109/ICIP.2001.958071.

Wikipedia (2007a). *Linear Interpolation*. URL: https://en.wikipedia.org/wiki/Linear{_}interpolation (visited on 2016-03-12).

Wikipedia (2007b). *Nearest-neighbor interpolation*. URL: https://en.wikipedia.org/wiki/Nearest-neighbor{_}interpolation (visited on 2016-03-18).

Wikipedia (2010). *Marching Cubes*. URL: https://en.wikipedia.org/wiki/Marching{_}cubes (visited on 2016-02-15).

Wikipedia (2013). *Lanczos resampling*. URL: https://en.wikipedia.org/wiki/Lanczos{_}resampling (visited on 2016-03-18).

World Health Organization (2007). "Vision 2020 The Right to Sight - Global Initiative for the Elimination of Avoidable Blindness: Action plan 2006-2001". *WHO Press, Ed.*

Yuan, X., X. Gu, J. S. Crabb, X. Yue, K. Shadrach, J. G. Hollyfield, and J. W. Crabb (2010). "Quantitative proteomics: comparison of the macular Bruch membrane/choroid complex from age-related macular degeneration and normal eyes." *Molecular & cellular proteomics : MCP* 9(6), pp. 1031–46. ISSN: 1535-9484. DOI: 10.1074/mcp.M900523-MCP200.

Zhou, J. and K. D. Tönnies (2003). "State of The Art for Volume Rendering". *Simulation*, pp. 1–29.